Magnetism in the $J_{\mathrm{eff}} = \frac{1}{2}$ kagome antiferromagnet Nd_3BWO_9: Thermodynamics, nuclear magnetic resonance, muon spin resonance, and inelastic neutron scattering studies

A. Yadav,[1] A. Elghandour,[2] T. Arh,[3] D. T. Adroja,[4,5] M. D. Le,[4] G. B. G. Stenning,[4] M. Aouane,[4] S. Luther,[6] F. Hotz,[7] T. J. Hicken,[7] H. Luetkens,[7] A. Zorko,[3,8] R. Klingeler,[2] and P. Khuntia[1,9,*]

[1]*Department of Physics, Indian Institute of Technology Madras, Chennai 600036, India*
[2]*Kirchhoff Institute of Physics, Heidelberg University, INF 227, D-69120 Heidelberg, Germany*
[3]*Jožef Stefan Institute, Jamova c. 39, SI-1000 Ljubljana, Slovenia*
[4]*ISIS Facility, Rutherford Appleton Laboratory, Chilton, Didcot, Oxon OX11 0QX, United Kingdom*
[5]*Highly Correlated Matter Research Group, Physics Department, University of Johannesburg, Auckland Park 2006, South Africa*
[6]*Dresden High Magnetic Field Laboratory (HLD-EMFL), Helmholtz-Zentrum Dresden-Rossendorf, 01328 Dresden, Germany*
[7]*Paul Scherrer Institute, Center for Neutron and Muon Sciences CNM, 5232 Villigen PSI, Switzerland*
[8]*Faculty of Mathematics and Physics, University of Ljubljana, Jadranska u. 19, SI-1000 Ljubljana, Slovenia*
[9]*Quantum Centre of Excellence for Diamond and Emergent Materials, Indian Institute of Technology Madras, Chennai 600036, India*

(Received 11 July 2024; revised 9 December 2024; accepted 5 February 2025; published 5 March 2025)

The intertwining of competing degrees of freedom, anisotropy, and frustration induced strong quantum fluctuations offers an ideal ground for realizing exotic quantum phenomena in the rare-earth based kagome lattice. Herein, we report the synthesis, structure, thermodynamic, muon spin relaxation (μSR), nuclear magnetic resonance (NMR), and inelastic neutron scattering (INS) studies of a frustrated quantum magnet Nd_3BWO_9 (NBWO), wherein Nd^{3+} ions constitute a distorted kagome lattice. The INS experiments on NBWO allow us to establish a detailed crystal electric field (CEF) spectrum. The magnetic susceptibility reveals the presence of two energy scales in agreement with the INS results, wherein the higher-energy state is dominated by the thermal population of CEF excitations. The lowest Kramers ground-state doublet is well separated from the excited state, suggesting that the compound realizes a low-energy $J_{\mathrm{eff}} = \frac{1}{2}$ state at low temperatures. The low-energy state is witnessed via thermodynamic results that reveal an anomaly at 0.3 K typical of a phase transition, which is attributed to the presence of complex magnetic ordering phenomena. The broad maximum in the specific heat well above 0.3 K indicates the presence of short-range spin correlations. The isothermal magnetization reveals a field-induced $\frac{1}{3}$ magnetization plateau at low temperatures. μSR relaxation rate experiments, on the other hand, neither show the signature of a phase transition nor spin freezing down to 34 mK. The zero-field μSR relaxation rate is governed by an Orbach process and reveals the presence of fluctuating moments owing to the depopulation of crystal field levels, reflected as a constant value of the relaxation rate in the temperature range $0.04 \leqslant T \leqslant 10$ K. NMR results indicate the presence of fluctuating Nd^{3+} moments down to 1.8 K, consistent with μSR experiments. Our comprehensive results reveal that a field-induced quantum phenomenon is at play, exemplifying the proximity effect of competing magnetic states and the coexistence of static and fluctuating moments along with short-range spin correlations in this frustrated kagome magnet. The broad rare-earth RE_3BWO_9 family of frustrated kagome magnets is a promising candidate for hosting exotic quantum states driven by spin-orbit coupling and frustration.

DOI: 10.1103/PhysRevB.111.094408

I. INTRODUCTION

Geometrically frustrated magnets, wherein the incompatibility of exchange interactions between the spins in minimizing the ground state energy leads to macroscopic ground-state degeneracy, nontrivial low-energy excitation spectra, and quantum phase transitions, represent a mainstream field of modern condensed matter [1]. Quantum mechanical effects such as spin-orbit coupling, entanglement, and quantum fluctuations, as well as the nontrivial topology of the electron wave function of frustrated quantum materials, offer an incredible ground to realize intriguing quantum and topological states such as quantum spin liquids (QSLs) with exotic quasiparticle excitations [2,3]. Quantum spin liquid is a highly entangled state of quantum matter wherein frustration-induced strong quantum fluctuations evade magnetic long-range ordering down to absolute zero temperature despite strong exchange interaction between spins. QSL is promising to host fractional excitations that are coupled to emergent gauge fields that has the potential to address some of the recurring themes in quantum condensed matter and is highly relevant for topological quantum computing [1–3]. In this context, the frustrated kagome antiferromagnet (AFM) with corner-sharing triangles of magnetic moments renders an emblematic two-dimensional model that

---

[*] Contact author: pkhuntia@iitm.ac.in

can maximize frustration induced quantum fluctuations and is a promising contender for hosting exotic quantum phenomena [4–10]. Quantum spin liquids [11–13], magnetization plateaus [14], incommensurate magnetic order [15], chiral spin-ordered states [16], massive Dirac fermions in ferromagnetic kagome metal, the anomalous Hall effect [17–19], the Berry phase [20], and unconventional superconductivity [21–22] in kagome magnets represent an appealing avenue in contemporary quantum matter to establish theoretical models that could resemble the properties of experimental candidates [23,24]. A weak perturbation in the nearest-neighbor Heisenberg model, such as next-nearest neighbor interactions, anisotropy, including the Dzyaloshinskii-Moriya interaction, in kagome magnets, can have a striking effect on the underlying spin Hamiltonian and ground-state properties [1,25–35]. Quantum criticality is also at play in diverse QSL models and frustrated magnets, suggesting that nonthermal external tuning parameters, i.e., pressure and magnetic field, can drive a quantum phase transition at $T \rightarrow 0$, exemplifying the competition between the nearly degenerate phases that have very similar characteristic energy scales [4–6,25,36].

A rare-earth based frustrated kagome quantum magnet with distinct magnetic ions is a promising candidate for stabilizing a structurally perfect lattice comprising the highly tunable nature of weak exchange interactions mediated by strongly localized magnetic moments. In these kagome materials, the synergistic interplay between strong spin-orbit coupling and the crystal electric field (CEF) often generates an exchange anisotropy, which often leads to effective spin-$\frac{1}{2}$ degrees of freedom that are prone to strong quantum fluctuations at low temperatures, thus offering an excellent route to stabilize a plethora of many-body quantum states [2–7,25,37–44]. However, defects and antisite disorder in many experimental frustrated magnets pose strong constraint for the unambiguous identification of exotic quantum state and associated magnetic excitations. The current challenge is to design, discover, and investigate structurally perfect kagome AFM representatives that provide a viable platform to realize fascinating quantum states. In this vein, the recently discovered rare-earth family RE_3BWO_9 (RE = rare-earth elements), where RE^{3+} ions form a distorted kagome lattice in the *ab* plane and are stacked along the *c* axis, provides a viable platform to realize spin-orbit driven correlated quantum states with nontrivial low-energy excitation spectra [45]. For instance, RE_3BWO_9 (RE = Gd, Dy, and Ho) shows a large magnetocaloric effect under the application of an external magnetic field, which is highly relevant for magnetic refrigeration at low temperatures. Pr_3BWO_9 exhibits a dynamic ground state down to 0.03 K with Ising-like spin correlations, while Sm_3BWO_9 hosts an incommensurate magnetic order. Nd_3BWO_9 (NBWO) is also a promising candidate to host frustration and field-induced quantum states, including a $\frac{1}{3}$ magnetization plateau, and unconventional quantum critical phenomena at low temperatures [46–51]. However, microscopic details concerning spin freezing, local magnetic field distribution at low temperatures, and a comprehensive CEF scheme are not yet clear for the kagome magnet NBWO. Moreover, detailed insights into the ground state properties by local probe techniques such as nuclear magnetic resonance (NMR) and muon spin relaxation (μSR) are still missing.

Herein, we present the synthesis, magnetization, specific heat, μSR, NMR, and inelastic neutron scattering (INS) results of polycrystalline sample of the spin-orbit driven frustrated $4f$ magnet NBWO. Our thermodynamic results reveal the realization of a $J_{\mathrm{eff}} = \frac{1}{2}$ state in the lowest Kramers doublet, which is well separated from the excited states, as confirmed by our INS experiments. Thermodynamic results reveal the presence of a weak AFM interaction between Nd^{3+} moments ($J_{\mathrm{eff}} = \frac{1}{2}$) at low temperatures. In addition, thermodynamic results suggest a magnetically ordered state at ∼0.3 K and short-range spin correlations above 0.8 K. The μSR results do not detect spin-freezing or magnetic ordering down to 34 mK, possibly related to structural distortion and the coexistence of static and fluctuating moments. The μSR relaxation rate is driven by an Orbach mechanism and dynamic electronic moments. NMR results are consistent with the thermodynamic and μSR results. The observation of a fractionalized magnetization plateau in the magnetization isotherm recorded at low temperatures suggests a complex magnetic ground state. Our comprehensive results indicate that an intriguing field-induced magnetic phenomenon is at play in this spin-orbit driven frustrated kagome magnet. The low-temperature magnetism is driven by static and fluctuating magnetic moments, along with short-range spin correlations.

II. EXPERIMENTAL DETAILS

Polycrystalline samples of NBWO were synthesized following a standard solid-state reaction route. Stoichiometric amounts of Nd_2O_3 (Alfa Aesar, 99.999%), H_3BO_3 (Alfa Aesar, 98%), and WO_3 (Alfa Aesar, 99.998%) were taken as starting materials [45,52]. Since H_3BO_3 is highly volatile, we have taken 5% of the excess to maintain proper stoichiometry in the sample. Nd_2O_3 was preheated at 900 °C overnight to remove moisture and carbonates prior to use. The reagents were thoroughly mixed to achieve better homogeneity. The pellets were annealed in an alumina crucible in the temperature range of 700–900 °C with several intermediate grindings. The nonmagnetic analog La_3BWO_9 used for inelastic scattering experiment was prepared following the same method. For INS experiments, boron-11-enriched samples were synthesized. The x-ray diffraction (XRD) data were taken on the polycrystalline sample of NBWO using a benchtop PANalytical diffractometer with Cu $K\alpha$ radiation ($\lambda = 1.541$ Å) at room temperature.

The dc magnetization measurements on NBWO were performed in the temperature range of $1.8 \leqslant T \leqslant 350$ K using a Magnetic Properties Measurement System (MPMS3, Quantum Design). For measurements down to 400 mK, the MPMS3 was equipped with the iQuantum He3 setup. The dc magnetization data were obtained following zero-field (ZF) and field-cooled protocols. The ac magnetization measurements were conducted in the temperature range from 1.8 to 60 K with 5–7 Oe ac excitation fields, up to 5 T dc magnetic fields, and frequencies ranging from 10 Hz to 0.8 kHz using the ac option of the MPMS3. To measure the specific heat of the sample, a thermal relaxation method was employed using the specific heat option of the Physical Property Measurement System (PPMS, Quantum Design). For NBWO, the specific heat measurements were carried out in the temperature range of 0.06–4 K using a dilution refrigerator in ZF on the PPMS. The pulsed-field magnetization measurements up to 60 T were performed at the Dresden High Magnetic Field Laboratory (HLD), using a compensated pickup-coil magnetometer in a coaxial geometry with a pulse raising time of 7 ms. Each measurement of the sample was followed by recording the background without a sample under identical conditions and its subsequent subtraction of the sample measurement to avoid any background contributions [53]. The pulsed-field magnetization data were calibrated using magnetization data recorded in the static magnetic field on the MPMS. The field dependence of magnetization obtained by the two methods is in good agreement, confirming the accuracy of our experiments.

INS measurements were carried out at the ISIS Neutron and Muon Source on the MARI time-of-flight spectrometer on NBWO powder samples with an enriched 11-B isotope. The experiments were carried out using a closed-cycle refrigerator and a Fermi chopper with the Gd-slit package. We collected data at 5 K with a neutron incident energy of $E_i = 80$ meV and a Fermi-chopper speed of 250 Hz. We also measured the phonon reference 11-B enriched compound La_3BWO_9 in identical conditions.

The μSR experiments were performed on GPS and FLAME spectrometers at the Swiss muon source at PSI in Villigen, Switzerland, in zero field (ZF) and longitudinal field (LF) configurations. The measurements on the GPS instrument were performed down to 1.6 K on a pressed pellet 10 mm in diameter and 1.6 mm thick. The pellet was secured between two 25 μm Cu foils and fastened to a copper fork sample holder. Additionally, the FLAME spectrometer equipped with a Variox plus Kevinox dilution fridge insert was used for ZF and LF μSR measurements in a wide temperature range between 0.034 and 300 K. The μSR data were analyzed to extract relevant parameters to shed insights into the ground-state properties of the present material using the MUSRFIT program [54].

Here, ^{11}B NMR ($I = \frac{3}{2}$) measurements were carried out using a home-built spectrometer and Oxford magnet with a fixed field of ∼9.4 T corresponding to a Larmor frequency of 128.321 MHz. A flow cryostat was used to cover the temperature range between 4 and 300 K. A 133 mg powder sample was used for these measurements. The NMR spectra were recorded by sweeping the frequency and combining individual spectra obtained via the standard Hahn-echo pulse sequence. The ^{11}B spin-lattice relaxation was measured by employing the inversion recovery pulse sequence.

III. RESULTS

A. Structural details

The XRD data taken at room temperature confirm the phase purity of the samples studied in this paper. To determine the structural parameters, Rietveld refinement of the XRD data was performed using GSAS software. The Rietveld refinement of the XRD data reveals no detectable atomic disorder in this material [Figs. 1(a) and 1(b)]. It reveals that NBWO crystallizes in a hexagonal structure with space group $P6_3$. In this material, Nd^{3+} ions constitute a distorted kagome spin-lattice in the *ab* plane that is stacked along the *c* axis. The refinement parameters are consistent with earlier reports [52] and are summarized in Table I. It is observed that the Nd^{3+} ions form NdO_8 dodecahedrons with oxygen ions which are distorted due to the slightly different Nd-O bond lengths, i.e., 2.7, 3, and 2.6 Å, resulting in a distorted kagome lattice in the *ab* plane, as shown in Fig. 1(a), that is consistent with previous reports [45,49,50,52]. The structure is distorted in the *ab* plane, as there are two inequivalent Nd triangles constituting the kagome network: one with an Nd-Nd bond length of ∼4.2 Å and one with a bond length of ∼4.9 Å. While the triangles are still corner shared, the interstitial region is not a regular hexagon in shape, as can be seen in Fig 1(a), which suggests a complex exchange network in this frustrated magnet. The presence of a structural phase transition has been ruled out by the specific heat result presented in Sec. III D.

B. Magnetization

The response of magnetization in the presence of an external applied magnetic field reveals interesting insights concerning exchange interactions, anisotropy, and spin correlations in NBWO. The temperature dependence of dc magnetic susceptibility measured in an external magnetic field of 0.1 T is shown in Fig. 1(c). The dc magnetic susceptibility shows neither a signature of long-range magnetic order nor spin freezing down to 1.8 K. The inverse dc magnetic susceptibility data show two energy scales, wherein the high-temperature $T > 150$ K behavior of inverse susceptibility corresponds to the thermal population of CEF excitations [25]. The inverse magnetic susceptibility shows a change of slope below 100 K, indicating repopulation of CEF levels. The Curie-Weiss fit (Fig. 1(c) inset) of inverse magnetic susceptibility data below 10 K yields an effective moment $\mu_{\rm eff} = 2.81(1)\ \mu_B$, which is small compared with the free ion moment value $\mu_{\rm eff}^{\rm free} = 3.62\ \mu_B$ of the Nd^{3+} ion ($4f^3$, $^4I_{9/2}$; $S = \frac{3}{2}$, $J = \frac{9}{2}$), indicating the realization of a low-energy state with $J_{\rm eff} = \frac{1}{2}$ at low temperatures that might support strong quantum fluctuations. The reduced effective moment that is obtained from the fit of inverse magnetic susceptibility at low temperatures indicates that only some crystal field levels contribute to the susceptibility below 10 K, and thus, there must be an energy gap between these low-lying levels and higher energy levels such that, above 150 K, we recover the full expected effective moment.

The corresponding Curie-Weiss temperature $\Theta_{\rm CW} = -1.20(2)$ K represents the energy scale of exchange interaction between Nd^{3+} ($J_{\rm eff} = \frac{1}{2}$) moments at low temperatures. The CEF affects the magnetic susceptibility at high temperatures in $4f$ magnets. In NBWO, it splits the tenfold degenerate $J = \frac{9}{2}$ multiplet into five Kramers doublets of the Nd^{3+} ion. The lowest Kramers doublet with $J_{\rm eff} = \frac{1}{2}$ at low temperatures is well separated from the excited states, as revealed by our INS experiments, as discussed in Sec. III C. The $J_{\rm eff} = \frac{1}{2}$ lowest Kramers state mainly governs the low-temperature physics of this frustrated magnet. The mean field approximation, $J_{\rm ex} = -\frac{3k_B\Theta_{\rm CW}}{zS(S+1)}$ (where $z = 4$ and $S = J_{\rm eff} = \frac{1}{2}$ in the present case) yields an AFM exchange interaction $J_{\rm ex}/k_B = 1.20(2)$ K. The presence of weak exchange interaction is typical of

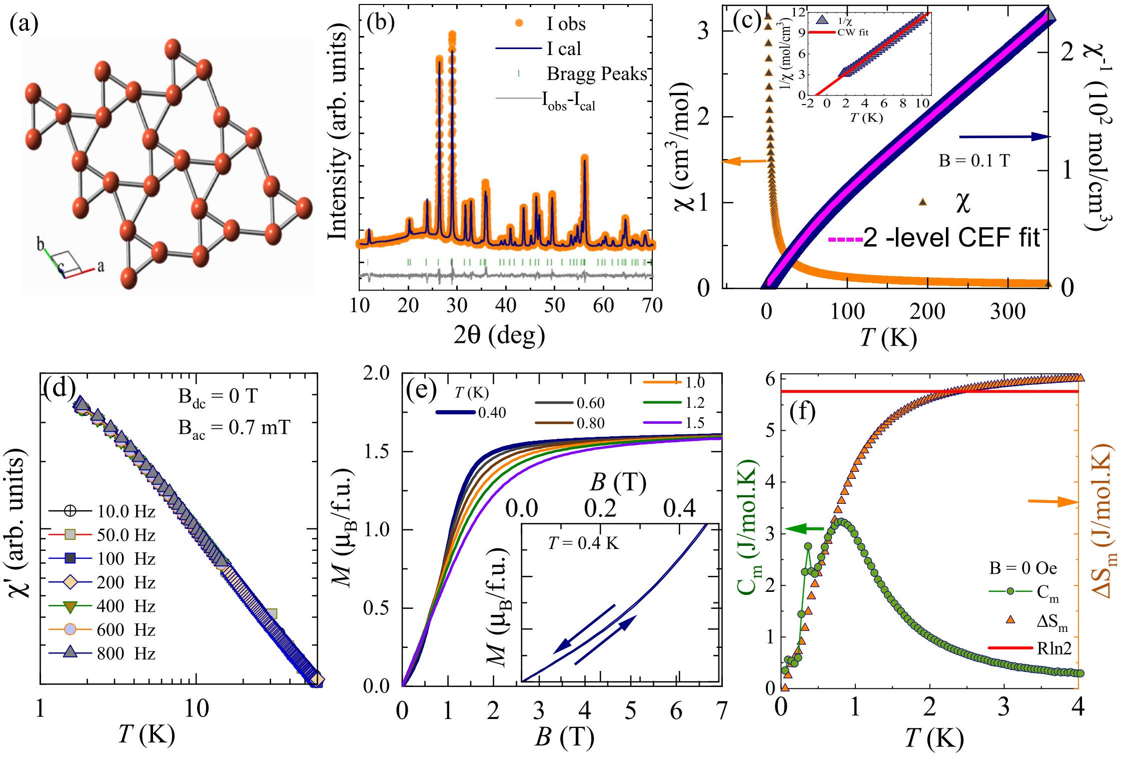

FIG. 1. (a) Kagome lattice constituted of Nd^{3+} ions in the *ab* plane of $\mathrm{Nd_3BWO_9}$. (b) Rietveld refinement of x-ray diffraction (XRD) data recorded at room temperature. (c) Temperature dependence of magnetic susceptibility in 0.1 T (left) taken in zero-field cooling (ZFC) mode and inverse magnetic susceptibility with Curie-Weiss and two level crystal electric field (CEF) fits, as discussed in the text (right). The inset show the fit of $1/\chi$ vs T at low temperatures. (d) Ac susceptibility recorded at different frequencies in zero dc field and 0.7 mT ac field. (e) Magnetization isotherms at several temperatures. The inset shows the low-field magnetization isotherm at 0.4 K for better clarity. (f) Temperature dependence of magnetic specific heat after subtracting the lattice ($\sim T^3$) and nuclear ($\sim T^{-2}$) contributions in zero field (ZF) at low temperature. The magnetic entropy in ZF that saturates to a value Rln2, reflecting the realization of a low-energy $J_{\text{eff}} = \frac{1}{2}$ Kramer doublet ground state at low temperatures in this $4f$ kagome magnet.

$4f$ magnets owing to strong localization of rare-earth ions that is comparable with the dipolar interaction [37]. Our low-temperature specific heat data reveal a phase transition ~0.3 K [see Fig. 1(f)], which is possibly due to an extra term in the magnetic Hamiltonian leading to complex magnetic ordering phenomena. The frustration parameter $f = \frac{|\Theta_{\text{CW}}|}{T_N}$, quantifying the degree of frustration, is thus ~5, suggesting a highly frustrated spin lattice that enhances quantum fluctuations, leading to suppressed magnetic ordering at ~0.3 K, as discussed in the following section.

As depicted in Fig. 1(c), the two energy scales in the inverse magnetic susceptibility of the Nd^{3+} ion could be reconciled using a simple two-level model, a simple approximation assuming that there are two levels [55] as described below:

$$\frac{1}{\chi(T)} = \frac{8(T - \Theta_{\text{CW}})[1 + \exp(-\Delta/k_BT)]}{\mu_{1\text{eff}}^2 + \mu_{2\text{eff}}^2 \exp(-\Delta/k_BT)},$$

where $\frac{\Delta}{k_B} = 215$ (10) K is the gap between the ground-state Kramers doublet and the first excited CEF level, $\mu_{1\text{eff}} = 3.01(1)\ \mu_B$ is the effective moment of the ground state, and $\mu_{2\text{eff}} = 4.20(2)\ \mu_B$ is the effective moment of the first excited state. The Curie-Weiss temperature $\Theta_{\text{CW}} = -1.50(2)$ K is related to the exchange interaction between Nd^{3+} moments in the Kramers ground state. The large value of CEF gap ($\frac{\Delta}{k_B}$), reflected as a change of slope

TABLE I. The atomic parameters obtained from the Rietveld refinement of XRD data of NBWO recorded at room temperature. (Space group: $P6_3$, $a = b = 8.6997(1)$ Å, $c = 5.5006(1)$ Å, $\alpha = \beta = 90°$, $\gamma = 120°$, and $\chi^2 = 1.7$, $R_{wp} = 4.78\%$, $R_p = 3.69\%$, and $R_{\text{exp}} = 3.66\%$).

Atom	Wyckoff position	x	y	z	Occupancy
Nd	6*c*	0.3590(2)	0.0832(1)	0.2292(2)	1
B	2*a*	0.0000	0.0000	0.7500	1
W	2*b*	0.3333	0.6666	0.2551(2)	1
O1	6*c*	0.1610(2)	0.0582(3)	0.8862(4)	1
O2	6*c*	0.1991(2)	0.4441(2)	0.0461(3)	1
O3	6*c*	0.0971(3)	0.4730(2)	0.5080(3)	1

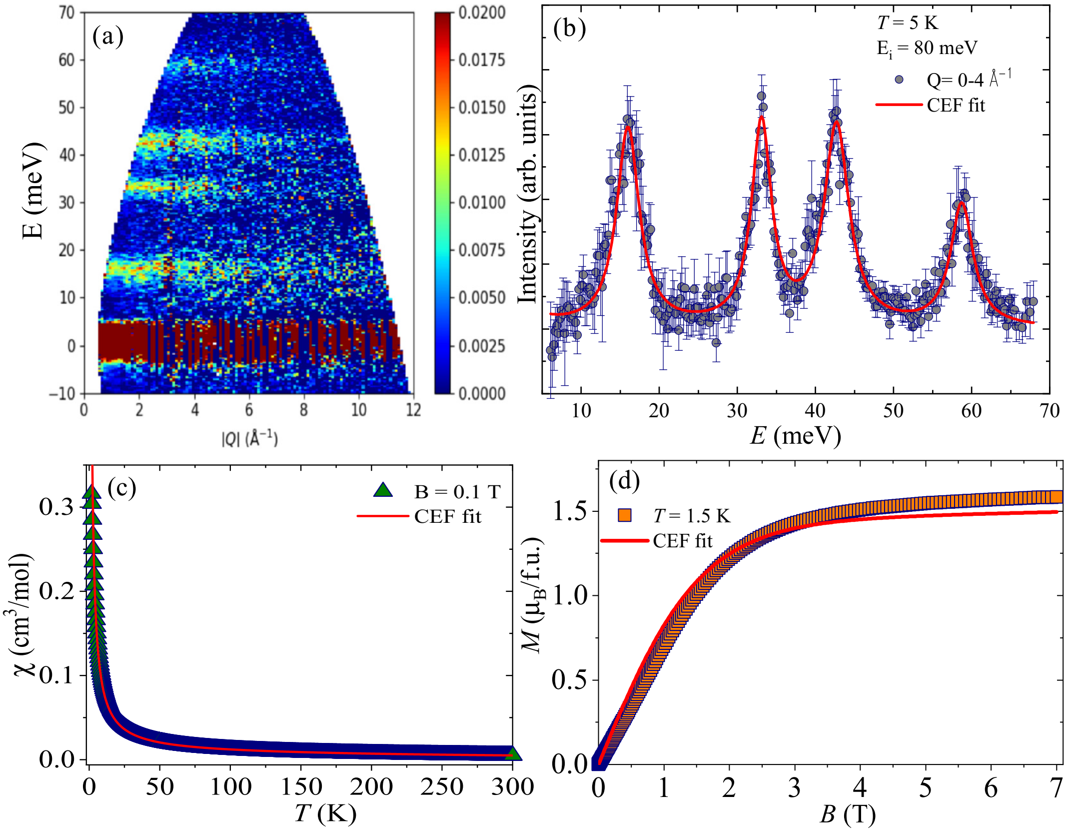

FIG. 2. (a) Inelastic neutron scattering (INS) intensity of Nd_3BWO_9 obtained after subtraction of phonon contribution using the nonmagnetic reference La_3BWO_9 at 5 K for the incident energy $E_i = 80$ meV. (b) Q-integrated (0–4 $Å^{-1}$) E vs intensity cut from the INS data taken with $E_i = 80$ meV at 5 K with fit to the crystal electric field (CEF) model shown by the solid line. (c) Temperature-dependence magnetic susceptibility data on the polycrystalline sample, and the solid line is the calculated magnetic susceptibility using the CEF parameters as provided in the appendix. (d) Field dependence of magnetization isotherm at 1.5 K, and the solid line corresponds to the calculated magnetization isotherm at 1.5 K with relevant CEF parameters.

of inverse susceptibility data below 100 K, suggests that the Kramers doublet ground state is well separated from the excited states, which is in reasonable agreement with that obtained from the INS experiment, as discussed in the next section. As shown in Fig. 1(d), the ac susceptibility at different frequencies rules out a spin-glass state down to 1.8 K. The absence of hysteresis in the magnetization isotherm at 400 mK [see Fig. 1(e)] adds further credence to the claim. In the absence of specific heat on the nonmagnetic analog, the magnetic specific heat in zero field obtained after subtracting the lattice ($C_L \sim T^3$) and nuclear specific heat ($C_N \sim 1/T^2$) shows a broad maximum ~0.8 K, and on further lowering the temperature, an AFM phase transition is observed at 0.3 K, as shown in Fig. 1(f). As presented in Fig. 1(f), the magnetic entropy extracted from the specific heat data saturates to a value that corresponds to Rln2 at low temperatures, suggesting the realization of a low-energy $J_{\rm eff} = \frac{1}{2}$ state in the ground state Kramers doublet, which is in agreement with magnetic susceptibility.

C. CEF spectrum

The magnetism of the frustrated kagome magnet NBWO is innately connected to the CEF scheme of the Nd^{3+} ion. To investigate the crystal field excitations and anisotropy and to probe the energy and wave vector dependence of the dynamic structure factor in NBWO, we have performed INS experiments on the MARI spectrometer [Fig. 2(a)]. Figure 2(b) shows the Q-integrated (0–4 $Å^{-1}$) INS spectra from low wave vector Q in NBWO. It shows magnetic scattering estimated after subtracting the phonon using the nonmagnetic La_3BWO_9 data [see Fig. 2(a)] [56]. We have observed four well-defined CEF excitations from the ground-state CEF doublet of Nd^{3+} (ground multiplet $J = \frac{9}{2}$, which spits into five CEF doublets in the C_1 point symmetry of Nd^{3+} ions in the paramagnetic state), in NBWO [Fig. 2(b)], which indicate the localized nature of $4f$ electron in this kagome magnet. The solid line shows the fit based on the CEF analysis, and the values of CEF parameters, energy eigenvalues and their wave functions obtained are given in Tables II–IV (see Appendix).

The CEF parameters were estimated by fitting the INS spectra and magnetization data taken on the polycrystalline sample together (see Appendix for more details). The calculated magnetic susceptibility along with the experimental susceptibility data are shown in Fig. 2(c). We also simulated the magnetization isotherm at 1.5 K using the CEF parameters, and the results are plotted in Fig. 2(d), which also agree reasonably well with the experimental M vs H results

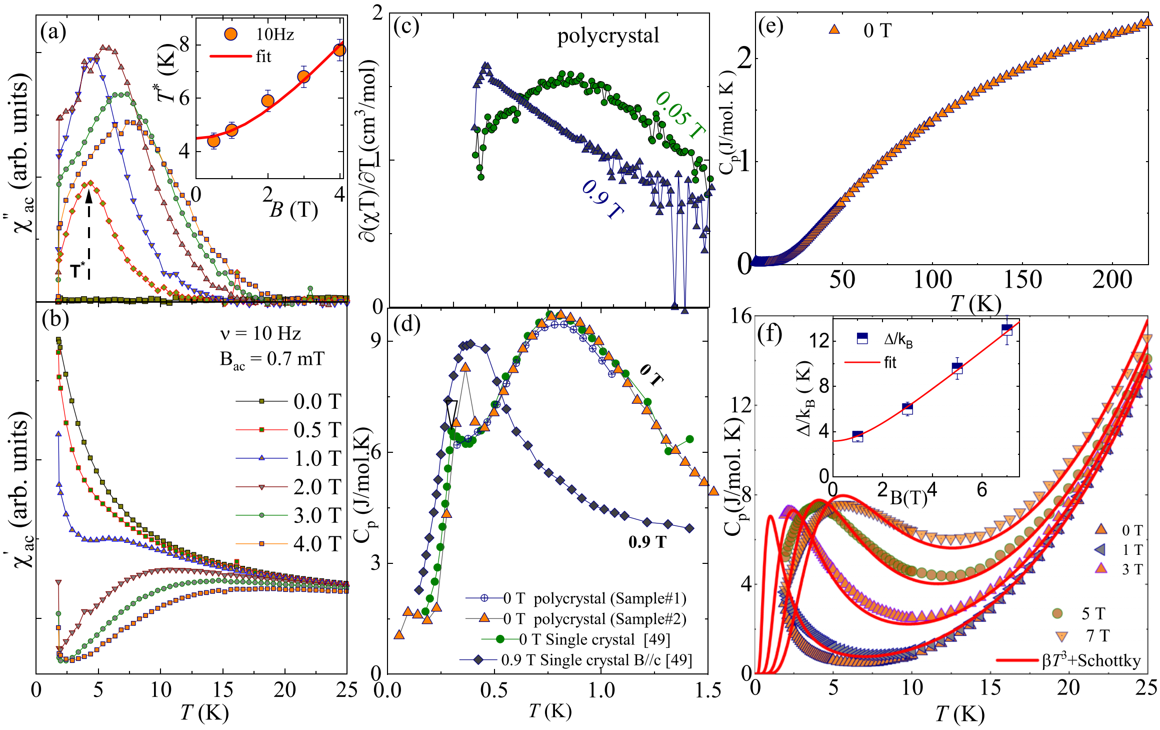

FIG. 3. (a) Temperature dependence of the imaginary part of the ac susceptibility, and the inset shows the variation of broad maxima (T*) in the imaginary part of ac susceptibility with the external dc magnetic field. The solid line is a fit, as discussed in the text. (b) Temperature dependence of the real part of the ac susceptibility in different dc fields taken at 10 Hz and an ac field 0.7 mT. (c) Temperature dependence of Fisher specific heat determined from dc susceptibility measured in 0.05 and 0.9 T. (d) Temperature dependence of specific heat in the polycrystalline samples of Nd_3BWO_9 that is compared with the single-crystal data adapted from Ref. [49]. (e) The temperature dependence of specific heat in zero field in the temperature range $1.8 \leqslant T \leqslant 220$ K rules out the presence of any structural phase transition. (f) Temperature dependence of specific heat taken in different applied fields at low temperature. The solid line is a fit to Schottky model plus the T^3 term accounting for the phonon contributions, as discussed in the text, and the inset shows the field dependence of the Zeeman gap with a fit, as discussed in the next.

of NBWO [50]. The value of the CEF gap of 186(8) K suggests that the lowest Kramers doublet is well separated from the excited states, confirming the thermodynamics and μSR results. Thus, the ground-state physics of this kagome AFM could be mapped by the low-energy state $J_{\mathrm{eff}} = \frac{1}{2}$, corroborating thermodynamic results. The $J_{\mathrm{eff}} = \frac{1}{2}$ state arises due to strong spin-orbit coupling and CEF induces strong quantum fluctuations at low temperatures and likely to dominate the ground state of this frustrated magnet.

D. AC susceptibility and specific heat

Ac susceptibility is a sensitive probe to track ground-state properties and spin dynamics in frustrated magnets. Ac susceptibility measurements were performed in zero dc field and in ac excitation magnetic fields in a wide frequency range (10 Hz to 800 Hz) to delineate spin dynamics and shed light onto field-induced effects in this kagome antiferromaget. As shown in Fig. 3(a), the real part of ac susceptibility (χ'_{ac}) recorded in an ac field of 7 Oe increases monotonically upon decreasing temperature without any signature of magnetic ordering down to 1.8 K, which is consistent with the dc magnetic susceptibility.

The frequency-independent behavior of ac susceptibility down to 1.8 K suggests that the characteristic fluctuation rate of Nd^{3+} moments is beyond the timescale of ac susceptibility experiment. Figures 3(a) and 3(b) depict the ac susceptibility taken in several dc fields with an ac excitation field of 7 Oe at a frequency 10 Hz. The real part of ac susceptibility (χ'_{ac}) in dc magnetic fields shows a field-induced behavior at ~7 K and a noticeable change of slope with strong dc fields [Fig. 3(b)]. Notably, the imaginary part of the ac susceptibility (χ''_{ac}) exhibits a broad maximum ~4.3 K in dc magnetic fields of 0.5 T, and the position of the maximum shifts toward higher temperature upon increasing magnetic field, suggesting the emergence of a field-induced gap. Contrastingly, the amplitude of χ''_{ac} starts decreasing with a dc magnetic field, $\mu_0 H \geqslant 2\,T$ [57]. The magnetic origin of the broad maximum in specific heat at ~0.8 K in ZF is confirmed by Fisher's specific heat [$\frac{\partial \chi T}{\partial T}$] calculated from the dc susceptibility recorded down to 0.4 K [see Fig. 3(c)]. It is worth noting that this maximum is independent of the measurement protocol (ZFC-FC) and is insensitive to magnetic field up to 0.1 T. However, the 0.8 K maximum flattens with magnetic field, $\mu_0 H > 0.4\,T$ and shifts toward lower temperature and completely disappears with a field, $\mu_0 H \geqslant 0.9\,T$. Interestingly, the magnetic specific heat shows an anomaly at ~0.4 K in a field of 0.9 T, which indicates that a field-induced phenomenon is at play in this kagome AFM. This is indeed consistent with the presence of an anomaly in isothermal magnetization recorded at low temperatures, as discussed in the next paragraph. To single out potential magnetic ordering, we have performed magnetization and specific heat measurements also in the sub-Kelvin temperature range, given the weak interaction energy scale in this localized $4f$ magnet.

Figure 3(d) depicts the temperature dependence of specific heat in sub-Kelvin temperature taken in ZF that is compared with that taken on the single crystals adapted from Ref. [49]. The specific heat shows a sharp anomaly at ~0.3 K, typical of long-range magnetic ordering. The anomaly at 0.3 K is sensitive to the applied magnetic field, and it smears out with the magnetic field. The specific heat shows a broad peak ~0.4 K in an external magnetic field of 0.9 T. The appearance of a broad maximum in specific heat ~0.8 K in the absence of a magnetic field and the lower value of magnetic entropy release ~2.5 J/mol K at the ordering temperature ~0.3 K compared with the expected value 5.76 J/mol K in ZF are characteristic features of short-range spin correlations. Furthermore, the position of the broad maximum in magnetic specific heat is in close agreement with that expected at $T/J_{\rm ex} \sim 0.6$ for an $S = J_{\rm eff} = \frac{1}{2}$ kagome quantum magnet, which adds further credence to the existence of short-range spin correlations [58,59]. The specific heat results indicate the coexistence of long- and short-range order in this kagome material. The specific heat in the temperature range from 1.8 to 220 K [see Fig. 3(e)] does not show any anomalies that suggest the absence of a structural phase transition in the temperature range of investigation in this material. Figure 3(f) shows the temperature dependence of specific heat in different external applied magnetic fields. As shown in Fig. 3(f), the broad maximum shifts in a Schottky-like manner toward higher temperature upon increasing the magnetic field. To get an estimate of the gap value owing to the Zeeman splitting of the lowest Kramers doublet in the presence of applied magnetic field, the specific heat data in the magnetic field are fitted with the two-level Schottky model and the T^3 term due to phonon contribution $C_p = \beta T^3 + C_{\rm Sch}$, with $C_{\rm Sch} = fR(\frac{\Delta}{k_BT})^2 \frac{\exp(\frac{\Delta}{k_BT})}{[1+\exp(\frac{\Delta}{k_BT})]^2}$, where f represents the fraction of paramagnetic $\rm Nd^{3+}$ ions participating in the splitting of the ground state doublet, R is the universal gas constant, Δ is the Zeeman gap, and k_B is the Boltzmann constant. The field-induced gap that scaled with the magnetic field is ascribed to the Zeeman splitting of the lowest Kramers doublet $J_{\rm eff} = \frac{1}{2}$ at low temperatures [inset of Fig. 3(f)]. To estimate the value of the field-induced gap, T^* vs H obtained from ac susceptibility [inset of Fig. 3(a)] and Δ vs H obtained from the Schottky model of the specific heat [inset of Fig. 3(f)] were fitted with ZF gap plus a Zeeman term in quadrature $\Delta(H) = \sqrt{\Delta_0^2 + (g\mu_BH)^2}$ [51]. The obtained Landé g factor is in close agreement with that found from the magnetization results.

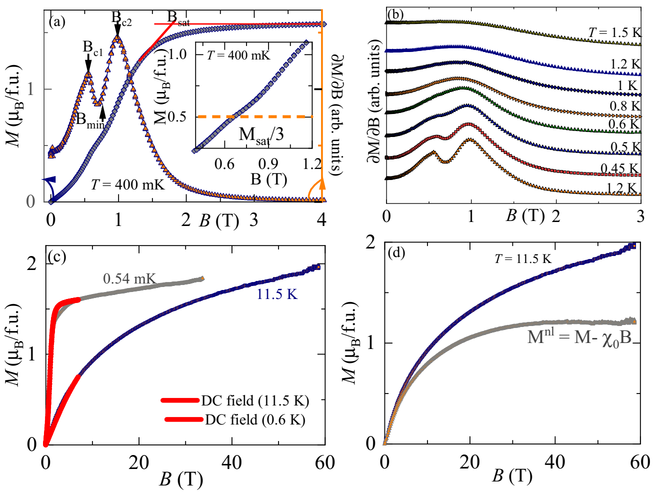

FIG. 4. (a) Magnetization isotherm recorded at 400 mK (left). The derivative of magnetization (∂M/∂B) with respect to magnetic field (right) is also shown to track the critical fields associated with some field-induced phases at low temperature. The inset shows the magnetization plateau at 400 mK. (b) Derivative of magnetization isotherms (∂M/∂B) taken at different temperatures to identify the evolution of field-induced phases in an external applied magnetic field. (c) Magnetization isotherm measured up to 60 T at different temperatures using a pulsed magnetic field. The pulsed field data are compared with that taken in a static magnetic field. (d) Magnetization isotherm at 11.5 K taken using a pulsed high-magnetic field up to 60 T, where $M^{nl} = M - \chi_0 B$ corresponds to nonlinear magnetization, as discussed in the text.

To shed more light onto the effect of the magnetic field on the low-temperature magnetic phase, we have performed magnetization measurements down to 400 mK and in magnetic fields up to 60 T. Figure 4(a) shows the isothermal magnetization recorded at 400 mK in NBWO. The absence of hysteresis rules out any secondary phases or spin-glass behavior in this frustrated kagome material. Magnetization increases with the field up to 0.4 T followed by a quasiplateau wherein the orientation of the magnetic moment changes much less with the external applied magnetic field. This is consistent with the $\frac{1}{3}$ $M_{\rm sat}$ magnetization plateau and eventually saturates to a value of $M_{\rm sat} = 1.5$ μ_B/Nd, as shown in Fig. 4(a), in line with what was found in the single crystals [49,50]. The observed features in the magnetization isotherm at 400 mK imply a complex magnetic structure wherein, phenomenologically, two spins in a triangle of the host kagome lattice might align with the external magnetic field, while one spin in each triangle points opposite to the applied magnetic field, known as the UUD phase. This exotic magnetic phase is associated with a complex magnetic phenomenon due to the fact that quantum fluctuations lift ground-state degeneracy and adopt specific spin configurations at low temperatures in frustrated magnets [1,60–64]. Upon further increase of the magnetic field, the magnetization isotherm at 400 mK saturates completely to a constant value ~1.5 $\mu_B/\rm Nd^{3+}$ in an external magnetic field of 4 T. The lower value of saturation magnetization than the expected value indicates the role of magnetic anisotropy or frustration-induced quantum fluctuations, as has been observed in several frustrated magnets [49,50,65,66]. As shown in Fig. 4(b), the derivative of isothermal magnetization ∂M/∂B at 400 mK reveals many interesting features, namely, a shoulderlike anomaly, two peaks corresponding to critical fields B_{c1}, B_{c2} related to the beginning and end of the magnetization plateau and a minimum at $B_{\rm min}$ at the center of the magnetization plateau [60–64]. The shoulderlike anomaly shifts to the lower magnetic field

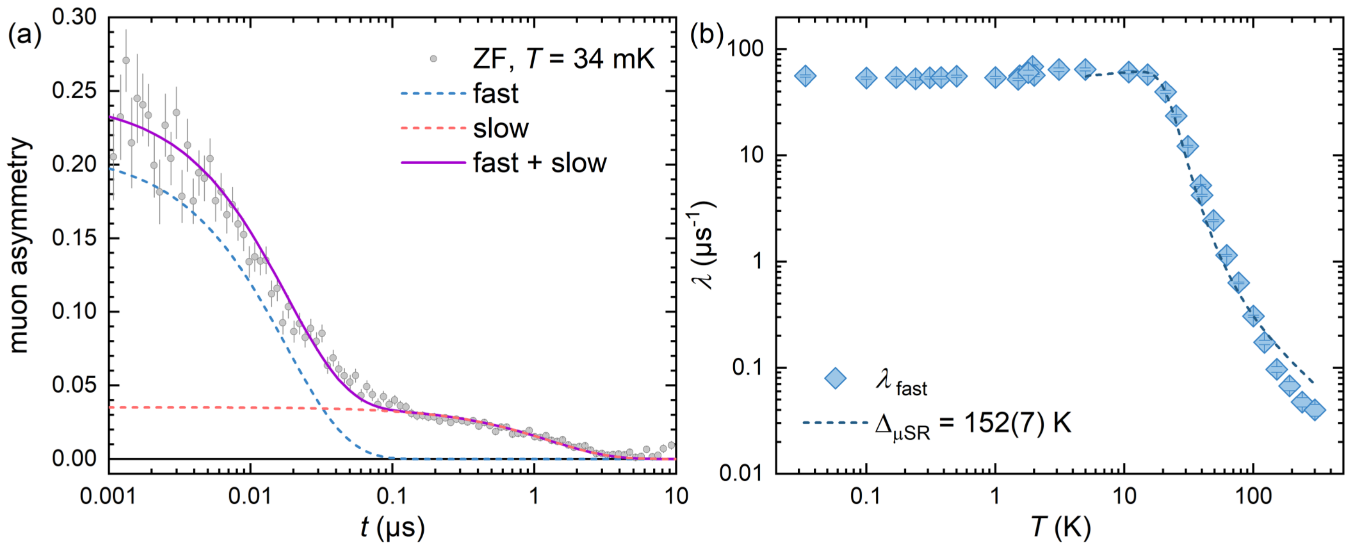

FIG. 5. (a) Zero-field (ZF) muon asymmetry dataset (points) at the base temperature with the two-component exponential fit (lines), as further explained in the text. (b) Temperature dependence of the ZF muon relaxation rate of the fast-relaxing dominant component. The dashed line depicts the model combining the temperature-independent and the Orbach relaxation mechanisms, as explained in the text.

side and vanishes upon increasing the temperature >0.5 K. The anomalies at B_{c1} and B_{min} slightly shift to the higher field side and eventually disappear at $T > 0.5$ K. The peak at B_{c2} shifts to the lower magnetic field side upon increasing the temperature and disappears within a broad hump at $T \geqslant 0.8$ K. This intriguing low-temperature behavior of the magnetization suggests that a complex field-induced quantum phenomenon such as metamagnetic mechanism is at play in this spin-orbit driven kagome AFM. Further experiments on the high-quality single crystals may shed interesting light onto this context.

Figures 4(c) and 4(d) represent a comparative account of the magnetization isotherms taken at different temperatures using a static field and a pulsed magnetic field up to 60 T. The magnetization isotherm at low temperature $T \sim 540$ mK saturates in the low-field regime and increases with field in the high-field limit [Fig. 4(c)]. The high-field magnetization isotherm at 11.5 K shows nonlinear behavior over a wide field range, as shown in Figs. 4(c) and 4(d). The linear term in the high-field magnetization isotherm indicates the presence of short-range spin correlations that are consistent with the enhancement of temperature dependence of magnetic susceptibility and NMR shift at low temperatures, as discussed in subsequent sections.

Remarkably, the specific heat C_p and Fisher specific heat derived from dc magnetic susceptibility $[\frac{\partial \chi T}{\partial T}]$ data show a broad maximum ~0.8 K, indicating a cross-over from a paramagnetic phase to a field-polarized state, consistent with our magnetization experiments conducted at low temperatures. Thermodynamic results suggest that the frustrated kagome material NBWO behaves like an unconventional paramagnet at $T > 0.8$ K.

E. Muon Spin Relaxation (μSR)

To shed additional light onto the magnetism of NBWO and track the local field distribution in real space as well as spin fluctuations, ZF and LF μSR experiments were conducted over wide temperature and field ranges.

1. *ZF measurements*

The μSR measurements were first performed in ZF with the initial spin direction antiparallel to the muon momentum. Figure 5(a) depicts the ZF muon asymmetry at the lowest temperature of 34 mK. The absence of oscillations in the ZF muon asymmetry curve and the vanishing asymmetry at long times, i.e., the absence of the $\frac{1}{3}$ tail, rules out static local magnetic fields at the muon stopping sites even at the lowest accessible temperature. The μSR asymmetry relaxes extremely quickly [note the logarithmic scale in Fig. 5(a)]; however, it is composed of two contributions: one faster and one slower decaying. Attempts to fit the data with the stretched exponent relaxation function were unsuccessful; a model with two simple exponentially decaying components works much better. Thus, we use the model $A(t) = A_0[f\exp(-\lambda_{\text{fast}}t) + (1-f)\exp(-\lambda_{\text{slow}}t)]$, with the fraction of the fast component $f = 0.86(1)$ fixed from low-temperature data. The presence of two components is likely due to muons stopping at two magnetically inequivalent muon stopping sites in the host spin lattice.

The temperature dependence of the μSR rate of the dominant fast component in ZF is shown in Fig. 5(b). The muon relaxation rate increases by several orders of magnitude on cooling the sample from 300 to 20 K, where a relaxation plateau is established. The strong temperature dependence of the ZF relaxation rate is consistent with an Orbach relaxation mechanism, associated with crystal field fluctuations, as observed in several frustrated magnets including $\text{NdTa}_7\text{O}_{19}$ [2,67].

Assuming the fast fluctuation regime, the muon relaxation rate is inversely proportional to the frequency of spin fluctuations $\lambda^{-1} \propto \nu_e$, which is described as a sum of two

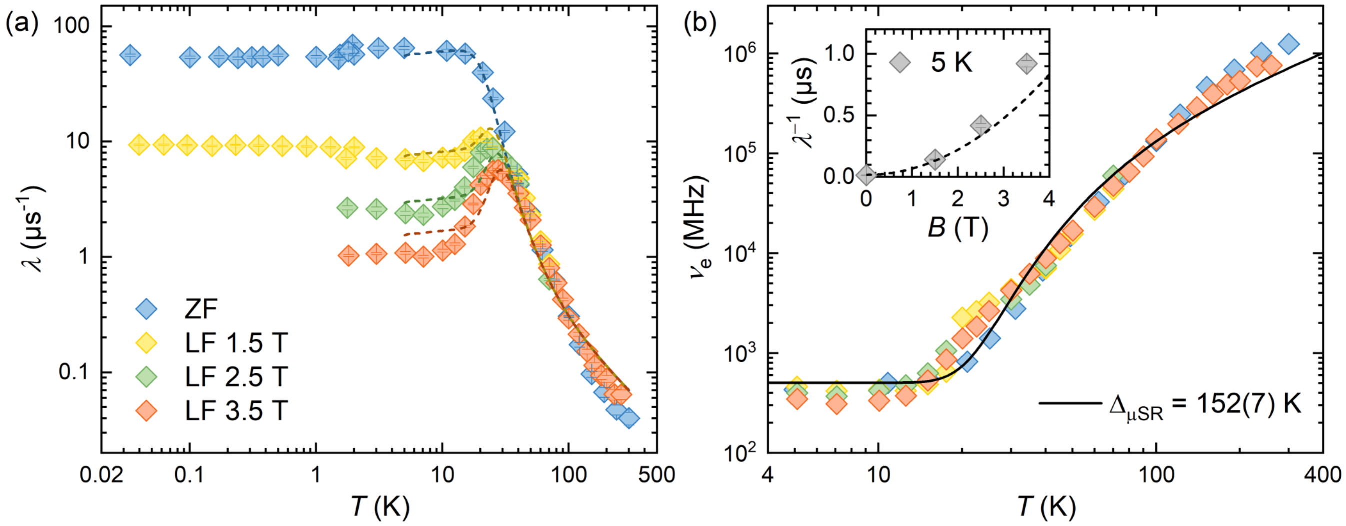

FIG. 6. (a) Temperature dependence of the muon spin relaxation (μSR) rate of the dominant fast component and (b) corresponding spin-fluctuation rate ν_e (see text) at zero field (ZF) and at several longitudinal fields (LFs). The inset shows the field dependence of the μSR rate at 5 K. The solid line in (b) is a fit of ν_e in all magnetic fields to Eq. (1). The obtained model is then used to calculate the relaxation rates with Eq. (2), which are shown with the dashed lines in (a) and the inset.

independent mechanisms,

$$\nu_e(T) = \nu_0 + \frac{\nu_1}{\exp(\Delta_{\mu\mathrm{SR}}/k_B T) - 1}. \qquad (1)$$

Here, the temperature-dependent term is the Orbach term that dominates the relaxation rate at $T > 20$ K. The constant term that corresponds to the relaxation rate plateau is associated with the μSR in the ground-state Kramers doublet. Such behavior of the relaxation rate suggests that, at temperatures $T < 20$ K, effective spin-$\frac{1}{2}$ degrees of freedom emerge in the ground state, as the excited crystal field states do not contribute any more to the μSR. The relaxation rate was modeled with Eq. (1) after combining the ZF and the LF measurements, which allowed for the determination of the coupling constant between λ^{-1} and ν_e, as shown in the next section. The fraction of the fast component is 86%, while the fraction of the slow component is just 14%. The relaxation rate of the slow component follows behavior akin to that of the fast component; however, the relaxation rate is one order of magnitude lower than that of the fast component (not shown here).

2. LF measurements

To gain more quantitative insight into the fluctuations of the Nd^{3+} magnetic moments, we performed LF measurements in a wide range of temperatures in three magnetic fields between 1.5 and 3.5 T.

The LF muon asymmetry curves were fitted with the same two-component exponential model as for ZF with the fraction of the two components fixed to $f = 0.86$, and the resulting fast-relaxing component is shown in Fig. 5(a). In the fast fluctuation regime, the field and temperature dependence of the relaxation rate is described by the Redfield model [68]

$$\frac{\lambda(T)}{\chi(T)T} = A_{\mu\mathrm{SR}}\frac{\nu_e(T)}{\nu_e(T)^2 + \omega_L^2}. \qquad (2)$$

Since the electron spin fluctuation frequency $\nu_e(T)$ monotonically increases with increasing temperature due to the Orbach process, a maximum appears in the μSR rate at a temperature where ν_e crosses the Larmor frequency $\omega_L = \gamma_\mu B_0$ for each LF [Fig. 6(a)]. From the maximum, we can extract the value of the coupling constant $A_{\mu\mathrm{SR}}$ for the three applied fields. It is found to be field independent within the error bars, so we use its average value $A_{\mu\mathrm{SR}} = 33.2 \times 10^3$ mol/(K cm^3 s^2) to derive the temperature dependence of $\nu_e(T)$ for each field including the ZF measurement. This rate is found to be field independent in the investigated range between 0 and 3.5 T [Fig. 6(b)].

The simultaneous fit of the four $\nu_e(T)$ datasets with a single-gap Orbach model plus a constant term [Eq. (1), three free parameters] yields a low-temperature plateau of $\nu_0 =$ 504(43) MHz and the gap of $\Delta_{\mu\mathrm{SR}}/k_B = 152(7)$ K that roughly matches the gap between the ground state and the first excited CEF level $\Delta/k_B = 186(8)$ K that was estimated via INS, again revealing that the lowest Kramers doublet is well separated from the excited Kramers doublets. A similar scenario was observed in several rare-earth-based frustrated magnets [25,67].

Finally, with the model for $\nu_e(T)$ and a coupling constant $A_{\mu\mathrm{SR}}$, we can use Eq. (2) to reconstruct the temperature dependence of the μSR data in all fields including ZF [Fig. 6(a)] as well as its field dependence at 5 K [inset in Fig. 6(b)]. Since we use a fairly simple model, the results at high temperatures are not described perfectly, likely due to higher CEF levels affecting the spin fluctuations, and there is some deviation at high fields as well. Nevertheless, the model is remarkably successful in describing the main features of the data in all fields. At low temperatures, the spin-fluctuating frequency $\nu_e = 504(43)$ MHz can be compared with the width of the fluctuating field distribution at the muon stopping site of $B_{\mathrm{loc}} = \gamma_\mu^{-1}\sqrt{A_{\mu\mathrm{SR}}\chi(T)T/2} = 0.14(4)$ T, which corresponds to $\gamma_\mu B_{\mathrm{loc}} = 119(36)$ MHz. The assumption of the fast

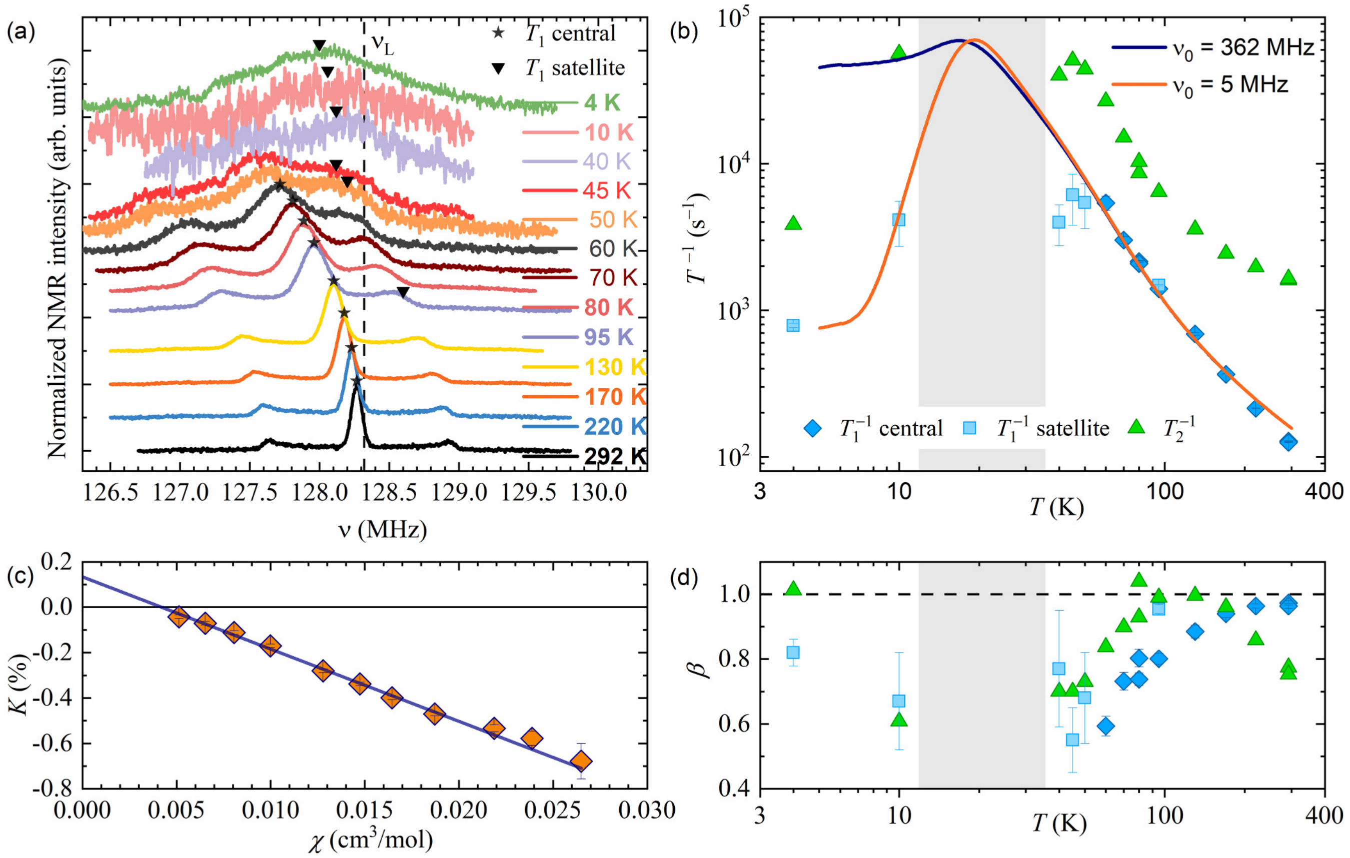

FIG. 7. (a) Temperature evolution of ^{11}B nuclear magnetic resonance (NMR) spectra recorded at 9.4 T. The dashed line corresponds to the Larmor frequency. Stars and triangles indicate the positions where T_1 measurements were conducted at a particular temperature. The scaling of the NMR shift of the central line with bulk susceptibility is shown in (c) together with the linear fit (solid line). (b) Temperature dependence of the spin-lattice ($1/T_1$) and spin-spin ($1/T_2$) relation rates and (d) corresponding stretch exponents. The solid lines in (b) correspond to the fits of the Bloembergen, Purcell, and Pound (BPP) model to the $1/T_1$ dataset, as explained in the text.

fluctuation regime ($\nu_e > \gamma_\mu B_{\text{loc}}$) was therefore justified even at low temperatures. It may be noted that μSR does not detect an anomaly at 0.3 K, unlike thermodynamic experiments. The absence of oscillations in μSR does not necessarily indicate the absence of long-range order. If slow magnetic fluctuations (in MHz) are present together with static magnetism, μSR might be dominated by the magnetic fluctuations at low temperatures. Therefore, our μSR study invokes the search for a persistent spin dynamic that coexists with the magnetic order indicated by the macroscopic techniques. Whether the emergence of exotic fractional excitations in frustrated magnets could lead to such a scenario is not clear at present, but it offers a direction to carry out detailed investigations on single crystals of NBWO in the future [69,70].

F. Nuclear Magnetic Resonance (NMR)

NMR is a powerful technique for providing microscopic insights into the intrinsic magnetic susceptibility and low-energy spin dynamics. In NBWO, there is only one crystallographic site for boron, with the Wyckoff position 2*a*. The ^{11}B NMR spectra shown in Fig. 7(a) consist of the central line and two satellite lines, as typical for $I = \frac{3}{2}$ nuclei. The quadrupole frequency $\nu_Q \approx 1.3$ MHz is determined from the distance between the two satellite peaks. The spectra get increasingly broadened with lowering temperatures; the change in the spectrum is especially large between 45 and 40 K. In the intermediate temperature range $10 \leqslant T \leqslant 40$ K, we cannot measure the NMR spectra due to extremely short spin-spin relaxation times T_2 [Fig. 7(b)]. Such NMR wipeout was observed before in another Nd-based kagome system, the neodymium langasite [71,72]. However, the NMR signal reappears at low temperatures $T < 10$ K due to the increase of the ^{11}B spin-spin relaxation time, in line with the slowing down of spin dynamics observed in μSR [Fig. 6(b)].

On cooling, the NMR spectra broaden and shift to lower frequencies. The ^{11}B NMR shift comprises temperature-dependent spin shift and temperature-independent orbital/chemical shift $K_0 = 0.13(1)\%$; $\mathrm{K}(T) = K_{\text{spin}} + K_0$. Here, K_{spin} scales with bulk magnetic susceptibility, i.e., $K_{\text{spin}}(T) = A_{hf}\chi(T)$, in the whole temperature range between 300 and 40 K, where the position of the central line can be unambiguously determined [Fig. 7(c)]. The fit yields the hyperfine coupling constant between nuclear and electronic spins $A_{hf} = -0.178(4)\ \mathrm{T}/\mu_{B.}$

To probe dynamic susceptibility associated with low-energy spin fluctuations, we also performed ^{11}B nuclear spin-lattice (T_1) relaxation time measurements [73]. The temperature dependence of the spin-lattice relaxation rate $1/T_1$ is shown in Fig. 7(b). Above 50 K, it was measured at the maximum of the central line [stars in Fig. 7(a)], for which the inversion recovery curve of the longitudinal nuclear magnetization M was fitted by a multiexponential recovery curve valid for magnetic relaxation in the case of $I = \frac{3}{2}$ nucleus,

$$M_z(t) = M_0\left[1 - (1+\alpha)\left\{0.1\exp\left[-\left(\frac{t}{T_1}\right)^{\beta}\right] + 0.9\ \exp\left[-\left(\frac{6t}{T_1}\right)^{\beta}\right]\right\}\right].$$

Here, α is the inversion factor, and β is the stretching exponent. The stretched exponential behavior [i.e., $\beta < 1$ in Fig. 7(d)] suggests a distribution of relaxation times in the host spin lattice. Below 50 K, $1/T_1$ was measured on the right satellite peak [triangles in Fig. 7(a)] due to better signal than the central line. Here, the magnetization was modeled with an expression appropriate for the satellite transition

$$M_z(t) = M_0\left[1 - (1+\alpha)\left\{0.1\exp\left[-\left(\frac{t}{T_1}\right)^{\beta}\right] + 0.5\exp\left[-\left(\frac{3t}{T_1}\right)^{\beta}\right] + 0.4\exp\left[-\left(\frac{6t}{T_1}\right)^{\beta}\right]\right\}\right].$$

To verify that the $1/T_1$ values from different parts of the spectra can be directly compared, we measured $1/T_1$ at both the central line and satellite transition at 95 K, where practically the same value was found [Fig. 7(d)].

The temperature dependence of $1/T_1$ matches the temperature dependence of the μSR rate λ [Fig. 6(a)]. In fact, we can use the same model as in the μSR analysis

$$\frac{1}{T_1 T\chi(T)} = A_{\rm NMR}\frac{\nu_e(T)}{\nu_e(T)^2 + \omega_L^2},$$

which is in NMR known as the Bloembergen, Purcell, and Pound (BPP) theory [73,74]. In our NMR experiment, we cannot measure the spin-lattice relaxation at the maximum value [where $\nu_e(T) = \omega_L$] because of the wipeout; therefore, the coupling constant $A_{\rm NMR}$ cannot be determined from the experiment, as it was possible for $A_{\mu\rm SR}$. Therefore, we use the same two-gap model with the parameters from the μSR modeling, with the rescaled $A_{\rm NMR} = 3500\ A_{\mu\rm SR}$ as the only free parameter. The resulting curve fits well with the experimental $1/T_1$ values in the temperature range between 300 and ~50 K [blue curve in Fig. 7(b)]. However, at low temperatures, this model fails to account for the experiment results. Better agreement is obtained [red curve in Fig. 7(b)] if the plateau value of the fluctuation frequency is also a free parameter when the fit yields $\nu_0 = 5(1)$ MHz. The decrease of the low-temperature fluctuation rate from $\nu_0 = 457(43)$ MHz, as determined from μSR, might be a result of a much stronger magnetic field applied in the NMR experiments (9.4 T) that should sufficiently polarize the spins at low temperatures. Alternatively, in the case of spin correlations, different local probes can filter spin fluctuations differently because of the site dependence of the form factor.

IV. DISCUSSION

Competing magnetic interactions and spin-orbit driven magnetic anisotropy conspire with quantum fluctuations in driving intriguing quantum phenomena in the present kagome antiferromagnet NBWO. The present kagome material is a distorted quantum magnet with corner-shared triangular motifs wherein inequivalent Nd-Nd bond distances and Nd-O-Nd bond angles most likely led to inequivalent exchange couplings in the host spin lattice. The kagome planes are separated by a distance comparable with the intraplane bond distance. In this material with $\rm Nd^{3+}$ ($^4\rm I_{9/2}$) ions, the crystal field states comprise five Kramers doublets, and the ground state with $J_{\rm eff} = \frac{1}{2}$ is well separated from the first excited state by a gap of 186(8) K, as evidenced by our INS experiments. The low-temperature physics of this kagome AFM is governed by the exchange interaction between $J_{\rm eff} = \frac{1}{2}$ moments. In the mean-field approximation, the AFM exchange interaction between $\rm Nd^{3+}$ moments determined from the Curie-Weiss temperature obtained from the fit of magnetic susceptibility at low temperatures is $J_{\rm ex} = 1.2(2)$ K. The presence of such a weak exchange interaction is typical of $4f$ magnetic moments in view of the strongly localized nature of $4f$ orbitals [2,3,25]. Specific heat measurements show a λ-like sharp anomaly ~0.3 K, implying an AFM phase transition that is associated with the presence of finite interplane interaction between $J_{\rm eff} = \frac{1}{2}$ spins [50]. The low-temperature magnetization isotherm in the magnetically ordered state exhibits a plateau at $\frac{1}{3}$ of the saturation magnetization value in the presence of an external magnetic field of ~0.5 $J_{\rm ex}$. This unconventional behavior of low-temperature magnetization isotherm in this frustrated kagome AFM is most likely related to a complex magnetic structure comprising up-up-down spin configurations of $J_{\rm eff} = \frac{1}{2}$ spins in the host spin lattice [60–64]. This type of magnetic behavior has been encountered in several frustrated $3d$ and $4f$ magnets with spontaneous breaking of translational symmetry [60–64]. In the $S = \frac{1}{2}$ Heisenberg model on a kagome lattice wherein spins interact via exchange coupling $J_{\rm ex}$, the $\frac{1}{3}$ magnetization plateau is characterized by low-energy excitations in the magnetically ordered state with a Zeeman gap that scales with magnetic field $B = 2J_{ex}S$, which is indeed relevant in the present case with $S = J_{\rm eff} = 1/2$ [1,60–64]. Notably, $S > \frac{3}{2}$ kagome lattices with Heisenberg exchange and strong easy axis or single-ion anisotropy show a magnetization plateau [60–64]. A broad maximum ~0.8 K in ZF specific heat and Fisher specific heat derived from dc magnetic susceptibility well above the transition temperature is close to that expected as per theoretical predictions $T/J_{\rm ex} \sim 0.6$ K for $S = J_{\rm eff} = \frac{1}{2}$ kagome magnets [58,59], which evinces short-range spin correlations in this frustrated magnet. The broad maximum in specific heat is sensitive to magnetic field, and an anomaly develops with an applied magnetic field of 0.9 T, which suggests that competing magnetic states are at play which are susceptible to external magnetic fields in the investigated frustrated magnet. The ZF μSR relaxation rate is governed by the Orbach mechanism typical of rare-earth-based frustrated magnets with CEF splitting with a gap that is consistent with thermodynamic and INS results. Here, ^{11}B NMR experiments unveil the presence of fluctuating electronic moments without the signature of magnetic ordering or freezing down to 1.8 K. The μSR asymmetry neither shows oscillations nor the $\frac{1}{3}$ tail down to 34 mK, ruling out the presence of long-range magnetic ordering and spin freezing, respectively, which is at variance with that observed in specific heat. The absence of oscillations in muon asymmetry does not necessarily precludes long-range magnetic order in this kagome magnet. One possible scenario could be that the coexistence of slow magnetic fluctuations along with static magnetism, and μSR might be dominated by the slowly fluctuating magnetic moments at low temperatures. Another possible scenario for the absence of an anomaly at 0.3 K in μSR results could be because the homogeneous internal field at the two muon stopping sites cancelled out. However, this seems unlikely, as both magnetically inequivalent sites would show this rather unusual effect simultaneously. A cancellation of dipolar fields arising from the ordered magnetic moments has indeed been observed, e.g., for a highly symmetric muon site in the heavy-fermion compound UPd_2Al_3 [75]. However, even in this case, a weak anomaly is observed at the transition temperature due to imperfections in the magnetic structure. One plausible scenario for the absence of oscillations in ZF muon asymmetry and no anomaly in μSR spin relaxation rate at $T \sim 300$ mK could be the fact that relaxation is possibly governed by the dipolar relaxation mechanism. Additionally, the structural distortion in the host spin lattice of this kagome magnet could amplify the distribution of internal fields with a zero average value at the muon site, leading to the absence of oscillations in muon asymmetry, as observed in several rare-earth based frustrated magnets [75–82]. Recently, a frustrated $4f$ magnet $YbBO_3$ has shown magnetic ordering in specific heat and neutron diffraction at ~0.4 K, which authors ascribed to the coexistence of long- and short-range ordering [81], whereas μSR detects no magnetic ordering down to 20 mK, possibly related to structural disorder [82]. However, in the present case, the exact origin of such a discrepancy is not clear at present, which should invoke further studies on high-quality single crystals of NBWO. An interesting query is whether such an intriguing low-temperature magnetic state could harbor exotic fractional excitations in this frustrated magnet, which is not obvious at present, but it provides a direction to carry out detailed investigations on the single crystals of NBWO in the future [60,61].

V. SUMMARY

The frustrated magnet NBWO with Nd^{3+} moments embodying a distorted kagome spin lattice is characterized by the interplay between spin-orbit coupling and spin correlations that leads to exotic magnetism and spin dynamics. The ground-state Kramers doublet is well separated from the excited states, implying that the ground state can be described by $J_{\text{eff}} = \frac{1}{2}$ spins, potentially leading to strong quantum fluctuations. The isothermal magnetization at sub-Kelvin temperature reveals a field-induced fractionalized magnetization plateau, suggesting an up-and-down ordered configuration of spins in each triangle of the frustrated kagome lattice with respect to the applied magnetic field. The specific heat, however, reveals the presence of a phase transition at 0.3 K that is attributed to the presence of interplane exchange interactions. The magnetic specific heat shows a broad maximum ~0.8 K, indicating the persistence of short-range spin correlations well above the magnetic phase transition temperature. The μSR relaxation at high temperatures is governed by an Orbach mechanism that is observed in several frustrated magnets based on rare-earth ions. In addition, the μSR and NMR experiments reveal the presence of fluctuating electronic moments. The absence of a $\frac{1}{3}$ tail in the muon asymmetry down to 34 mK rules out spin freezing in this frustrated magnet, which is consistent with thermodynamic results. The absence of long-range magnetic ordering down to 34 mK, as revealed by our ZF μSR experiments, suggests the predominant role of slowly fluctuating magnetic moments along with static magnetism at low temperatures. Furthermore, a weaker dipolar relaxation mechanism and structural distortion might explain the absence of oscillations in the ZF μSR asymmetry. A clear picture concerning this warrants a thorough μSR investigation on high-quality single crystals of NBWO. The external magnetic field drives several field-induced phases, implying the presence of a complex magnetic ordering phenomenon at temperatures $T < 0.3$ K in this spin-orbit driven frustrated magnet. Our results suggest that competing magnetic states are active, which are sensitive to external magnetic fields, and that the low-temperature physics is governed by static and fluctuating magnetic moments, along with short-range spin correlations in this kagome AFM. Further studies on the single crystals focusing on the effect of external perturbations such as chemical and hydrostatic pressure may provide vital clues concerning the exotic magnetism and spin dynamics in this class of frustrated magnets. The current family of spin-orbit-driven rare-earth based distorted kagome series RE_3BWO_9 offers a viable ground for the experimental realization of exotic quantum states and the establishment of a realistic microscopic Hamiltonian in this class of quantum materials.

ACKNOWLEDGMENTS

P.K. acknowledges funding by the Science and Engineering Research Board and Department of Science and Technology, India, through research grants. A.Y. thanks M. Barik for the help in synthesizing a batch of polycrystalline samples. A.Z. acknowledges the financial support of the Slovenian Research and Innovation Agency through Programme No. P1-0125 and Projects No. J1-50008 and No. N1-0148. R.K. and A.E. acknowledge the financial support by DFG under Germany's Excellence Strategy No. EXC2181/1–390900948 (the Heidelberg STRUCTURES Excellence Cluster) and through the DAAD GSSP program. D.T.A. acknowledges funding from EPSRC-UK (Grant No. EP/W00562X/1). We acknowledge PSI for beam time proposals. Experiments at the ISIS Neutron and Muon Source were supported by Beamtime Allocation No. RB2220746 from the Science and Technology Facilities Council. We acknowledge

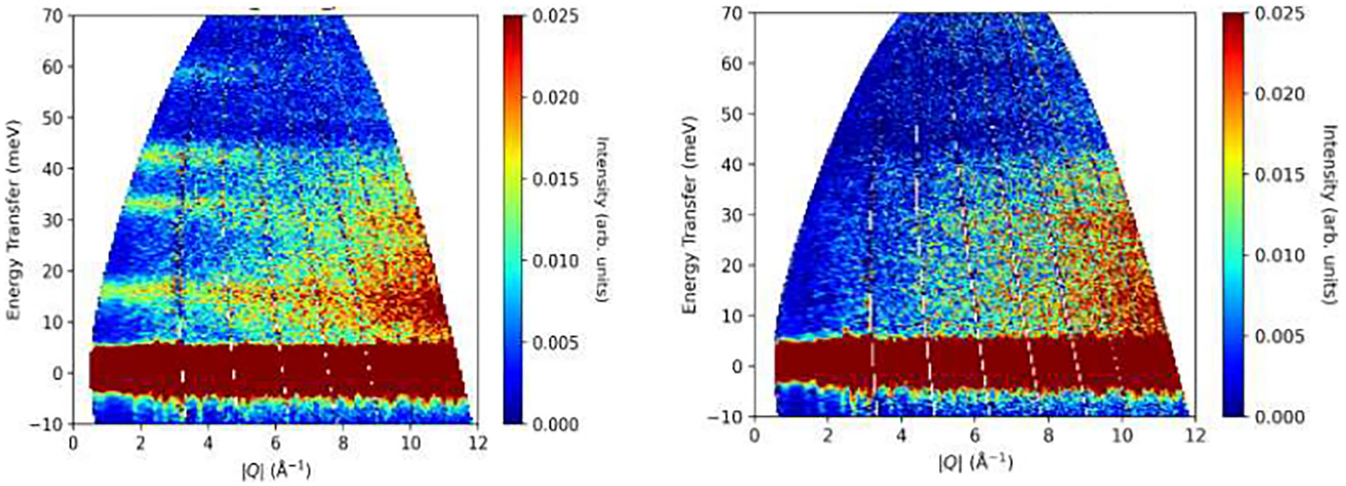

FIG. 8. (a) Inelastic neutron scattering intensity of (a) Nd_3BWO_9 and (b) the nonmagnetic reference La_3BWO_9 at 5 K for the incident energy $E_i = 80$ meV. The four crystal electric field (CEF) excitations are clearly visible after subtraction of phonon contribution using the nonmagnetic reference La_3BWO_9, as shown in Fig. 2(a).

the support of the HLD at HZDR, a member of the European Magnetic Field Laboratory.

DATA AVAILABILITY

The neutron scattering data that support the findings of this paper are openly available [83]. All other data are available from the corresponding author upon reasonable request.

TABLE II. The values of the CEF parameters in meV. The I before the parameters (i.e., IB_2^1) indicates that they are imaginary terms (sometimes called sine terms).

$B_2^0 = 0.0633$
$B_2^1 = 0.2997$
$B_2^2 = -0.1193$
$B_4^0 = -0.0010$
$B_4^1 = -0.0246$
$B_4^2 = -0.0054$
$B_4^3 = 0.0505$
$B_4^4 = -0.0046$
$B_6^0 = 0.0009$
$B_6^1 = 0.0008$
$B_6^2 = 0.0010$
$B_6^3 = 0.0014$
$B_6^4 = 0.0005$
$B_6^5 = -0.0047$
$B_6^6 = 0.0015$

$IB_2^1 = -0.2500$
$IB_2^2 = -0.2409$
$IB_4^1 = -0.0157$
$IB_4^2 = 0.0153$
$IB_4^3 = 0.0512$
$IB_4^4 = -0.0190$
$IB_6^1 = 0.0001$
$IB_6^2 = 0.0009$
$IB_6^3 = 0.0020$
$IB_6^4 = -0.0007$
$IB_6^5 = 0.0002$
$IB_6^6 = -0.0015$

APPENDIX

INS: CEF parameters

In this appendix, we discuss the CEF parameters obtained from simultaneously fitting the INS spectra at 5 K and magnetic susceptibility data. The crystal structure of Nb_3BWO_9 is hexagonal; however, the point symmetry of the Nd ion is triclinic C_1. Due to the low point symmetry of the Nd ion, the CEF Hamiltonian has a total of 27 independent CEF parameters. This makes it challenging to estimate all CEF parameters by fitting the INS data only. However, as we observed all four possible excitation peaks, we can use a variational method to fit the energy levels by varying the eigenvectors of the crystal field Hamiltonian [84]. We thus used this method in a Monte Carlo procedure to generate random starting parameters, which approximately give the observed energy levels Fig. 8. These parameters were then used in a Levenberg-Marquardt fit of the measured INS data. From these, we obtained 16 sets of CEF parameters which fit the INS data well. The calculated magnetic susceptibilities for all parameter sets were almost identical and match the measured data well, but the calculated magnetization varied, with disparate parameters yielding different saturation magnetization than the expected value. We thus chose the parameter set which gave the saturation closest to that measured. Values of the obtained CEF parameters are given in Tables II–IV.

TABLE III. CEF energy levels (in meV) for the CEF model.

E_0	E_1	E_2	E_3	E_4
0	15.9	33.1	42.7	58.7

TABLE IV. The orthogonalized eigenstates $\pm\omega_n$ ($n = 0 - 4$) of the CEF Hamiltonian in the $|\pm m_J\rangle$ basis and the corresponding eigenenergies of the $^4I_{9/2}$ Nd^{3+} multiplet in the kagome magnet NBWO. Note that the coefficients of the second (denoted $-$) level are the complex conjugates of the first (denoted $+$).

$\lvert\pm m_J\rangle$	$\pm\omega_0$	$\pm\omega_1$	$\pm\omega_2$	$\pm\omega_3$	$\pm\omega_4$
$\lvert\pm\frac{9}{2}\rangle$	$-0.2108+0.1388i$	$0.3361-0.2143i$	$-0.0145-0.3490i$	$-0.1366+0.2284i$	$0.1816-0.2528i$
$\lvert\pm\frac{7}{2}\rangle$	$0.0789-0.0444i$	$0.2387+0.0589i$	$0.1825+0.4934i$	$0.1078-0.2271i$	$0.0894-0.4466i$
$\lvert\pm\frac{5}{2}\rangle$	$-0.2452+0.0522i$	$-0.4643+0.3539i$	$0.1669-0.2219i$	$-0.0631+0.0567i$	$-0.1009-0.1217i$
$\lvert\pm\frac{3}{2}\rangle$	$0.0109+0.2281i$	$-0.2041-0.1794i$	$0.3587+0.1479i$	$0.1155+0.1594i$	$-0.1031+0.2261i$
$\lvert\pm\frac{1}{2}\rangle$	$-0.0920+0.0463i$	$-0.1276+0.2147i$	$-0.2903+0.2352i$	$-0.4476+0.2294i$	$0.1961-0.0773i$
$\lvert\mp\frac{1}{2}\rangle$	$0.1826-0.4044i$	$-0.1768-0.0653i$	$-0.0433+0.0793i$	$-0.4566+0.2022i$	$0.0039-0.0052i$
$\lvert\mp\frac{3}{2}\rangle$	$0.1564+0.5485i$	$-0.0926-0.0058i$	$0.1719-0.2319i$	$-0.1273+0.0810i$	$0.2487-0.3479i$
$\lvert\mp\frac{5}{2}\rangle$	$-0.2773-0.0335i$	$-0.1736-0.2561i$	$-0.2242-0.0037i$	$0.1174-0.2930i$	$0.2474-0.3197i$
$\lvert\mp\frac{7}{2}\rangle$	$0.1528+0.2194i$	$0.2013+0.1255i$	$0.1193+0.1531i$	$-0.2958-0.2415i$	$0.0957+0.2521i$
$\lvert\mp\frac{9}{2}\rangle$	$-0.2847-0.2228i$	$0.2764+0.1763i$	$-0.0153-0.2333i$	$-0.1114-0.1926i$	$-0.2633-0.2758i$
E (meV)	0	15.9	33.1	42.7	58.7

[1] *Introduction to Frustrated Magnetism: Materials, Experiments, Theory*, edited by C. Lacroix, P. Mendels, and F. Mila (Springer, New York, 2011).

[2] L. Balents, Spin liquids in frustrated magnets, Nature (London) **464**, 199 (2010).

[3] J. Khatua, B. Sana, A. Zorko, M. Gomilšek, K. Sethupathi, M. R. Rao, M. Baenitz, B. Schmidt, and P. Khuntia, Experimental signatures of quantum and topological states in frustrated magnetism, Phys. Rep. **1041**, 1 (2023).

[4] W. Witczak-Krempa, G. Chen, Y. B. Kim, and L. Balents, Correlated quantum phenomena in the strong spin-orbit regime, Annu. Rev. Condens. Matter Phys. **5**, 57 (2014).

[5] M. Vojta, Frustration and quantum criticality, Rep. Prog. Phys. **81**, 064501 (2018).

[6] H. Takagi, T. Takayama, G. Jackeli, G. Khaliullin, and S. E. Nagler, Kitaev quantum spin liquid—Concept and materialization, Nat. Rev. Phys. **1**, 264 (2019).

[7] C. Broholm, R. J. Cava, S. A. Kivelson, D. G. Nocera, M. R. Norman, and T. Senthil, Quantum spin liquids, Science **367**, eaay0668 (2020).

[8] L. Savary and L. Balents, Quantum spin liquids: A review, Rep. Progr. Phys. **80**, 016502 (2017).

[9] Y. Zhou, K. Kanoda, and T.-K. Ng, Quantum spin liquid states, Rev. Modern Phys. **89**, 025003 (2017).

[10] X.-G. Wen, Choreographed entanglement dances: Topological states of quantum matter, Science **363**, eaal3099 (2019).

[11] S. Yan, D. A. Huse, and S. R. White, Spin-liquid ground state of the $S = \frac{1}{2}$ kagome Heisenberg antiferromagnet, Science **332**, 1173 (2011).

[12] P. Khuntia, M. Velazquez, Q. Barthélemy, F. Bert, E. Kermarrec, A. Legros, B. Bernu, L. Messio, A. Zorko, and P. Mendels, Gapless ground state in the archetypal quantum kagome antiferromagnet $ZnCu_3(OH)_6Cl_2$, Nat. Phys. **16**, 469 (2020).

[13] K. Matan, T. Ono, Y. Fukumoto, T. J. Sato, J. Yamaura, M. Yano, K. Morita, and H. Tanaka, Pinwheel valence-bond solid and triplet excitations in the two-dimensional deformed kagome lattice, Nat. Phys. **6**, 865 (2010).

[14] S. Ishiwata, D. Wang, T. Saito, and M. Takano, High-pressure synthesis and structure of $SrCo_6O_{11}$: Pillared kagomé lattice system with a $\frac{1}{3}$ magnetization plateau, Chem. Mater. **17**, 2789 (2005).

[15] Z. Guguchia, H. Zhou, C. N. Wang, J.-X. Yin, C. Mielke III, S. S. Tsirkin, I. Belopolski, S.-S. Zhang, T. A. Cochran, T. Neupert *et al.*, Multiple quantum phase transitions of different nature in the topological kagome magnet $Co_3Sn_{2-x}In_xS_2$, npj Quantum Mater. **6**, 50 (2021).

[16] S. S. Gong, W. Zhu, L. Balents, and D. N. Sheng, Global phase diagram of competing ordered and quantum spin-liquid phases on the kagome lattice, Phys. Rev. B **91**, 075112 (2015).

[17] L. Ye, M. Kang, J. Liu, F. von Cube, C. R. Wicker, T. Suzuki, C. Jozwiak, A. Bostwick, E. Rotenberg, D. C. Bell *et al.*, Massive Dirac fermions in a ferromagnetic kagome metal, Nature (London) **555**, 638 (2018).

[18] D. Guterding, H. O. Jeschke, and R. Valentí, Prospect of quantum anomalous Hall and quantum spin Hall effect in doped kagome lattice Mott insulators, Sci. Rep. **6**, 25988 (2016).

[19] A. Petrescu, A. A. Houck, and K. L. Hur, Anomalous Hall effects of light and chiral edge modes on the Kagomé lattice, Phys. Rev. A **86**, 053804 (2012).

[20] X. Li, J. Koo, Z. Zhu, K. Behnia, and B. Yan, Field-linear anomalous Hall effect and Berry curvature induced by spin chirality in the kagome antiferromagnet Mn_3Sn, Nat. Commun. **14**, 1642 (2023).

[21] H. Chen *et al.*, Roton pair density wave in a strong-coupling kagome superconductor, Nature (London) **599**, 222 (2021).

[22] Z. Guguchia, R. Khasanov, and H. Luetkens, Unconventional charge order and superconductivity in kagome-lattice systems as seen by muon-spin rotation, npj Quantum Mater. **8**, 41 (2023).

[23] G. Semeghini, H. Levine, A. Keesling, S. Ebadi, T. T. Wang, D. Bluvstein, R. Verresen, H. Pichler, M. Kalinowski, R. Samajdar

et al., Probing topological spin liquids on a programmable quantum simulator, Science **374**, 1242 (2021).

[24] A. Hutter, J. R. Wootton, and D. Loss, Parafermions in a kagome lattice of qubits for topological quantum computation, Phys. Rev. X **5**, 041040 (2015).

[25] T. Arh, B. Sana, M. Pregelj, P. Khuntia, Z. Jagličić, M. D. Le, P. K. Biswas, P. Manuel, L. Mangin-Thro, A. Ozarowski *et al.*, The Ising triangular-lattice antiferromagnet neodymium heptatantalate as a quantum spin liquid candidate, Nat. Mater. **21**, 416 (2022).

[26] G. Misguich and P. Sindzingre, Magnetic susceptibility and specific heat of the spin-$\frac{1}{2}$ Heisenberg model on the kagome lattice and experimental data on $ZnCu_3(OH)_6Cl_2$, Eur. Phys. J. B **59**, 305 (2007).

[27] B. Bernu, L. Pierre, K. Essafi, and L. Messio, Effect of perturbations on the kagome $S = \frac{1}{2}$ antiferromagnet at all temperatures, Phys. Rev. B **101**, 140403(R) (2020).

[28] R. R. P. Singh, Valence bond glass phase in dilute kagome antiferromagnets, Phys. Rev. Lett. **104**, 177203 (2010).

[29] O. Cepas, C. M. Fong, P. W. Leung, and C. Lhuillier, Quantum phase transition induced by Dzyaloshinskii-Moriya interactions in the kagome antiferromagnet, Phys. Rev. B **78**, 140405(R) (2008).

[30] A. Zorko, M. Herak, M. Gomilšek, J. van Tol, M. Velázquez, P. Khuntia, F. Bert, and P. Mendels, Symmetry reduction in the quantum kagome antiferromagnet herbertsmithite, Phys. Rev. Lett. **118**, 017202 (2017).

[31] P. Mendels, F. Bert, M. A. de Vries, A. Olariu, A. Harrison, F. Duc, J. C. Trombe, J. S. Lord, A. Amato, and C. Baines, Quantum magnetism in the paratacamite family: Towards an ideal kagomé lattice, Phys. Rev. Lett. **98**, 077204 (2007).

[32] T. Arh, M. Gomilsek, P. Prelovsek, M. Pregelj, M. Klanjsek, A. Ozarowski, S. J. Clark, T. Lancaster, W. Sun, J.-X. Mi *et al.*, Origin of magnetic ordering in a structurally perfect quantum kagome antiferromagnet, Phys. Rev. Lett. **125**, 027203 (2020).

[33] T. F. Seman, C.-C. Chen, R. R. P. Singh, and M. van Veenendaal, The many faces of quantum kagome materials: Interplay of further-neighbour exchange and Dzyaloshinskii-Moriya interaction, arXiv:1508.01523.

[34] J. Colbois, B. Vanhecke, L. Vanderstraeten, A. Smerald, F. Verstraete, and F. Mila, Partial lifting of degeneracy in the $J_1 - J_2 - J_3$ Ising antiferromagnet on the kagome lattice, Phys. Rev. B **106**, 174403 (2022).

[35] W.-J. Hu, W. Zhu, Y. Zhang, S. Gong, F. Becca, and D. N. Sheng, Variational Monte Carlo study of a chiral spin liquid in the extended Heisenberg model on the kagome lattice, Phys. Rev. B **91**, 041124(R) (2015).

[36] Y. Tokiwa, C. Stingl, M.-S. Kim, T. Takabatake, and P. Gegenwart, Characteristic signatures of quantum criticality driven by geometrical frustration, Sci. Adv. **1**, e1500001 (2015).

[37] B. Gao *et al.*, Experimental signatures of a three-dimensional quantum spin liquid in effective spin-$\frac{1}{2}$ $Ce_2Zr_2O_7$ pyrochlore, Nat. Phys. **15**, 1052 (2019).

[38] Z.-F. Ding, Y.-X. Yang, J. Zhang, C. Tan, Z.-H. Zhu, G. Chen, and L. Shu, Possible gapless spin liquid in the rare-earth kagome lattice magnet $Tm_3Sb_3Zn_2O_{14}$, Phys. Rev. B **98**, 174404 (2018).

[39] Z. Ma, Z.-Y. Dong, S. Wu, Y. Zhu, S. Bao, Z. Cai, W. Wang, Y. Shangguan, J. Wang, K. Ran *et al.*, Disorder-induced spin-liquid-like behavior in kagome-lattice compounds, Phys. Rev. B **102**, 224415 (2020).

[40] A. Zorko, F. Bert, P. Mendels, P. Bordet, P. Lejay, and J. Robert, Easy-axis kagome antiferromagnet: Local-probe study of $Nd_3Ga_5SiO_{14}$, Phys. Rev. Lett. **100**, 147201 (2008).

[41] Z. Hu, Z. Ma, Y.-D. Liao, H. Li, C. Ma, Y. Cui, Y. Shangguan, Z. Huang, Y. Qi, W. Li *et al.*, Evidence of the Berezinskii-Kosterlitz-Thouless phase in a frustrated magnet, Nat. Commun. **11**, 5631 (2020).

[42] W.-Y. Su, F. Hu, C. Cheng, and N. Ma, Berezinskii-Kosterlitz-Thouless phase transitions in a kagome spin ice by a quantifying Monte Carlo process: Distribution of Hamming distances, Phys. Rev. B **108**, 134422 (2023).

[43] A. Julku, G. M. Bruun, and P. Törmä, Quantum geometry and flat band Bose-Einstein condensation, Phys. Rev. Lett. **127**, 170404 (2021).

[44] K. Górnicka, M. J. Winiarski, D. I. Walicka, and T. Klimczuk, Superconductivity in a breathing kagome metals ROs_2 (R = Sc, Y, Lu), Sci. Rep. **13**, 16704 (2023).

[45] M. Ashtar, J. Guo, Z. Wan, Y. Wang, G. Gong, Y. Liu, Y. Su, and Z. Tian, A new family of disorder-free rare-earth-based kagome lattice magnets: Structure and magnetic characterizations of RE_3BWO_9 (RE = Pr, Nd, Gd–Ho) boratotungstates, Inorg. Chem. **59**, 5368 (2020).

[46] L.-L. Li, X.-Y. Yue, W.-J. Zhang, H. Bao, D.-D. Wu, H. Liang, Y.-Y. Wang, Y. Sun, Q.-J. Li, and X.-F. Sun, Magnetism and giant magnetocaloric effect in rare-earth-based compounds R_3BWO_9 (R = Gd, Dy, Ho), Chin. Phys. B **30**, 077501 (2021).

[47] K.-Y. Zeng, F. Y. Song, Z. M. Tian, Q. Chen, S. Wang, B. Liu, S. Li, L. S. Ling, W. Tong, L. Ma *et al.*, Local evidence for collective spin excitations in the distorted kagome antiferromagnet Pr_3BWO_9, Phys. Rev. B **104**, 155150 (2021).

[48] K. Y. Zeng, F. Y. Song, L. S. Ling, W. Tong, Shiliang Li, Z. M. Tian, Long Ma, and Li Pi, Incommensurate magnetic order in Sm_3BWO_9 with distorted kagome lattice, Chin. Phys. Lett. **39**, 107501 (2022).

[49] D. Flavian, J. Nagl, S. Hayashida, M. Yan, Q. Zaharko, T. Fennell, D. Khalyavin, Z. Yan, S. Gvasaliya, and A. Zheludev, Magnetic phase diagram of the breathing-kagome antiferromagnet Nd_3BWO_9, Phys. Rev. B **107**, 174406 (2023).

[50] F. Song, H. Ge, A. Liu, Y. Qin, Y. Han, L. Ling, S. Yuan, Z. Ouyang, J. Sheng, L. Wu *et al.*, Magnetic field tuned anisotropic quantum phase transition in the distorted kagome antiferromagnet Nd_3BWO_9, Phys. Rev. B **108**, 214410 (2023).

[51] J. Nagl, D. Flavián, S. Hayashida, K. Yu. Povarov, M. Yan, N. Murai, S. Ohira-Kawamura, G. Simutis, T. J. Hicken, H. Luetkens *et al.*, Excitation spectrum and spin Hamiltonian of the frustrated quantum Ising magnet Pr_3BWO_9, Phys. Rev. Res. **6**, 023267 (2024).

[52] V. A. Krut'ko, A. A. Belik, and G. V. Lysanova, Structures of nonlinear hexagonal boratotungstates Ln_3BWO_9 (Ln = La, Pr, Nd, Sm, Gd, Tb, Dy), Russ. J. Inorg. Chem. **51**, 884 (2006).

[53] Y. Skourski, M. D. Kuz'min, K. P. Skokov, A. V. Andreev, and J. Wosnitza, High-field magnetization of Ho_2Fe_{17}, Phys. Rev. B **83**, 214420 (2011).

[54] A. A. Suter and B. M. Wojek, MUSRFIT: A free platform-independent framework for μSR data analysis, Phys. Proc. **30**, 69 (2012).

[55] T. Besara, M. S. Lundberg, J. Sun, D. Ramirez, L. Dong, J. B. Whalen, R. Vasquez, F. Herrera, J. R. Allen, M. W. Davidson *et al.*, Single crystal synthesis and magnetism of the BaLn_2O$_4$ family (Ln = lanthanide), Prog. Solid State Chem. **42**, 23 (2014).

[56] P. Khuntia and D. T. Adroja, *Novel Ground State in the Rare-Earth Based Kagome Antiferromagnets:* R_3BWO$_9$ (R = Pr, Nd) (STFC ISIS Neutron and Muon Source, Oxfordshire, 2023).

[57] A. Elghandour, Ph.D. Thesis, Thermodynamic and Magnetic Studies on Correlated Electron Systems with Competing Interactions, University of Heidelberg, Heidelberg, 2023.

[58] N. Elstner and A. P. Young, Spin-Heisenberg antiferromagnet on the kagome lattice: High-temperature expansion and exact-diagonalization studies, Phys. Rev. B **50**, 6871 (1994).

[59] J. Schnack, J. Schulenburg, and J. Richter, Magnetism of the $N = 42$ kagome lattice antiferromagnet, Phys. Rev. B **98**, 094423 (2018).

[60] J. Dorier, K. P. Schmidt, and F. Mila, Theory of magnetization plateaux in the Shastry-Sutherland model, Phys. Rev. Lett. **101**, 250402 (2008).

[61] A. Sen, K. Damle, and A. Vishwanath, Magnetization plateaus and sublattice ordering in easy-axis kagome lattice antiferromagnets, Phys. Rev. Lett. **100**, 097202 (2008).

[62] M. J. R. Hoch, H. D. Zhou, E. Mun, and N. Harrison, Pulsed field magnetization in rare-earth Kagome systems, J. Phys.: Condens. Matter **28**, 046001 (2016).

[63] A. Honecker, J. Schulenburg, and J. Richter, Magnetization plateaus in frustrated antiferromagnetic quantum spin models, J. Phys.: Condens. Matter **16**, S749 (2004).

[64] A. Sen, F. Wang, K. Damle, and R. Moessner, Triangular and kagome antiferromagnets with a strong easy-axis anisotropy, Phys. Rev. Lett. **102**, 227001 (2009).

[65] M. C. Hatnean, M. R. Lees, O. A. Petrenko, D. S. Keeble, G. Balakrishnan, M. J. Gutmann, V. V. Klekovkina, and B. Z. Malkin, Structural and magnetic investigations of single-crystalline neodymium zirconate pyrochlore $Nd_2Zr_2O_7$, Phys. Rev. B **91**, 174416 (2015).

[66] F. A. Cevallos, S. Guo, and R. J. Cava, Magnetic properties of lithium-containing rare earth garnets $Li_3RE_3Te_2O_{12}$ (RE = Y, Pr, Nd, Sm-Lu), Mater. Res. Express **5**, 126106 (2018).

[67] R. Orbach, Spin-lattice relaxation in rare-earth salts, Proc. R. Soc. Lond. A **264**, 458 (1961).

[68] A. Yaouanc and P. Dalmas de Réotier, *Muon Spin Rotation, Relaxation, and Resonance: Applications to Condensed Matter* (Oxford University Press, Oxford, 2011).

[69] L. Balents, M. P. A. Fisher, and S. M. Girvin, Fractionalization in an easy-axis kagome antiferromagnet, Phys. Rev. B **65**, 224412 (2002).

[70] B. Canals, I. A. Chioar, V.-D. Nguyen, M. Hehn, D. Lacour, F. Montaigne, A. Locatelli, T. O. Menteş, B. S. Burgos, and N. Rougemaille, Fragmentation of magnetism in artificial kagome dipolar spin ice, Nat. Commun. **7**, 11446 (2016).

[71] A. Zorko, F. Bert, P. Mendels, A. Potočnik, A. Amato, C. Baines, K. Marty, P. Bordet, P. Lejay, E. Lhotel *et al.*, Quantum tunneling in half-integer-spin kagome-lattice langasites, arXiv:1210.8187.

[72] M. Ulaga, J. Kokalj, A. Wietek, A. Zorko, and P. Prelovšek, Finite-temperature properties of the easy-axis Heisenberg model on frustrated lattices, Phys. Rev. B **109**, 035110 (2024).

[73] T. Moriya, *Spin Fluctuations in Itinerant Electron Magnetism* (Springer, Berlin, 1985).

[74] N. Bloembergen, E. M. Purcell, and R. V. Pound, Nuclear magnetic relaxation, Nature (London) **160**, 475 (1947).

[75] A. Amato, R. Feyerherm, F. N. Gygax, A. Schenck, M. Weber, R. Caspary, P. Hellmann, C. Schank, C. Geibel, and F. Steglich, Magnetic and superconducting properties of the heavy-fermion superconductor UPd_2Al_3, Eur. Phys. Lett. **19**, 127 (1992).

[76] D. T. Adroja, A. Bandyopadhyay, H. Leutkens, T. J. Hicken, J. A. Krieger, G. B. Stenning, Z. Tian, and S. Li (private communications).

[77] S. J. Blundell, I. M. Marshall, W. Hayes, and F. L. Pratt, Muon spin relaxation in $DyVO_4$ and $TbVO_4$, Phys. Rev. B **70**, 212408 (2004).

[78] J. S. Gardner, S. R. Dunsiger, B. D. Gaulin, M. J. P. Gingras, J. E. Greedan, R. F. Kiefl, M. D. Lumsden, W. A. MacFarlane, N. P. Raju, J. E. Sonier *et al.*, Cooperative paramagnetism in the geometrically frustrated pyrochlore antiferromagnet $Tb_2Ti_2O_7$, Phys. Rev. Lett. **82**, 1012 (1997).

[79] N. Hamaguchi, T. Matsushita, N. Wada, Y. Yasui, and M. Sato, Low-temperature phases of the pyrochlore compound $Tb_2Ti_2O_7$, Phys. Rev. B **69**, 132413 (2004).

[80] P. J. Baker, M. J. Matthews, S. R. Giblin, P. Schiffer, C. Baines, and D. Prabhakaran, Unusual field dependence of spin fluctuations on different timescales in $Tb_2Ti_2O_7$, Phys. Rev. B **86**, 094424 (2012).

[81] G. Sala, M. B. Stone, S.-H. Do, K. M. Taddei, Q. Zhang, G. B. Halász, M. D. Lumsden, A. F. May, and A. D. Christianson, Structure and magnetism of the triangular lattice material $YbBO_3$, J. Phys.: Condens. Matter **35**, 395804 (2023).

[82] K. Somesh, S. S. Islam, S. Mohanty, G. Simutis, Z. Guguchia, Ch. Wang, J. Sichelschmidt, M. Baenitz, and R. Nath, Absence of magnetic order and emergence of unconventional fluctuations in the $J_{\text{eff}} = \frac{1}{2}$ triangular-lattice antiferromagnet $YbBO_3$, Phys. Rev. B **107**, 064421 (2023).

[83] P. Khuntia and D. T. Adroja, https://doi.org/10.5286/ISIS.E.RB2220746.

[84] D. J. Newman and B. Ng, *Crystal Field Handbook* (Cambridge University Press, Cambridge, 2000).